SACS2 Final Report by GECO
July 12, 2002

Document Contact

Trygve Randen
Schlumberger Stavanger Research
Risabergveien 3, Tananger
P.O. Box 8013
4068 Stavanger
Norway
Tel.: +47 51 94 64 71
Mob.: +47 402 47 478
E-mail: trygve.randen@slb.com

List of authors (alphabetic)

Hilde Grude Borgos
Geir Vaaland Dahl
Kristine Årland Halvorsen
Terje Iversen
Magne Lygren
Michael Nickel
Trygve Randen
Thorleif Skov
Bent Audun Tjøstheim

Table of contents

WP 8-11 – Geophysical Interpretation

Lead by GECO

As evident from this report, seismic data is very well suited to mapping the presence and distribution of injected CO_2 in the sub-surface. The CO_2 acts as a very good "contrast agent" for the seismic signal. Questions of interest are thus: Can we make account for all the injected gas (with high confidence) and can we, from the seismic data, explain the migration path of the gas? The latter question has turned out to be very important in order to integrate seismic time lapse measurements with the reservoir model.

Several attempts are being taken to answer these questions and will be reported in the subsequent sections. First, the CO_2 is most likely constrained in its vertical movement by thin shale layers within the Utsira sand. Furthermore, migration through to the overlying sand wedge is observed. It is not straightforward to explain the observed migration by data from the baseline seismic survey. Next, making account for the injected gas is a very complex task, with large uncertainties. In this document, we report on several approaches to estimate the CO_2 present according to the time-lapse seismic data.

As already mentioned, the SACS2 project has clearly revealed the value of seismic data for monitoring the CO_2. However, if CO2 injection is rolled out in large scale, it will be of significant importance to develop an efficient workflow for the data analysis. Powerful tools will be necessary to ensure the efficiency. Consequently a significant research and technology development (RTD) effort is being devoted to the creation of efficient tools for the purpose.

Repeatability analysis

Time-lapse seismic data has the potential of identifying and pinpointing subtle changes that have occurred in e.g. a hydrocarbon reservoir during the time interval in question, at a distance of several kilometres underneath the seabed or earth surface. However, care must be taken in the analysis of the seismic data, as changes in the response may originate from several different sources. Typical reservoir parameters that will induce changes in the seismic response are changes in the fluid saturation levels, changes in rock porosity, as well as changes in reservoir pressure and temperature.

The changes in the seismic response may also be related to changes in the acquisition parameters. Examples of such parameters are the number of streamers, the spatial positioning of the hydrophones or geophones, the cable lengths, the source type and the ability of these sources to repeat the wavelets that are transmitted down the sub-surface. It is the aim to minimise the effects of the changes in acquisition parameters, in order to relate changes in the seismic response to the changes in reservoir parameters. Hence, the seismic processing of time-lapse data aims at maximising the repeatability of the different surveys, by using a range of different signal processing techniques. In order to validate the repeatability, and to improve our understanding of the available seismic data, repeatability assessments are presented below.

Relative time shift analysis

The seismic signal should not change above the Utsira Formation unless the CO_2 has leaked from the Utsira Formation to these areas. A good measure of the repeatability of the data sets will hence be obtained through an analysis of the seismic signal in the overburden.

In order to analyse the repeatability of the two seismic surveys, a set of reflectors in the overburden was interpreted on both seismic surveys. Figure 1 shows the time differences for some reflectors over, inside and below the Utsira Formation. On the time difference along the seabed, the acquisition footprint is clearly visible. However, this feature is gradually reduced further down in the section, and about 200 ms above the Utsira Formation it has almost vanished. This is due to a time shift compensation that was undertaken in the processing of the seismic data. The compensation was based on swath dependent time shifts in the range between 800 and 1200 ms.
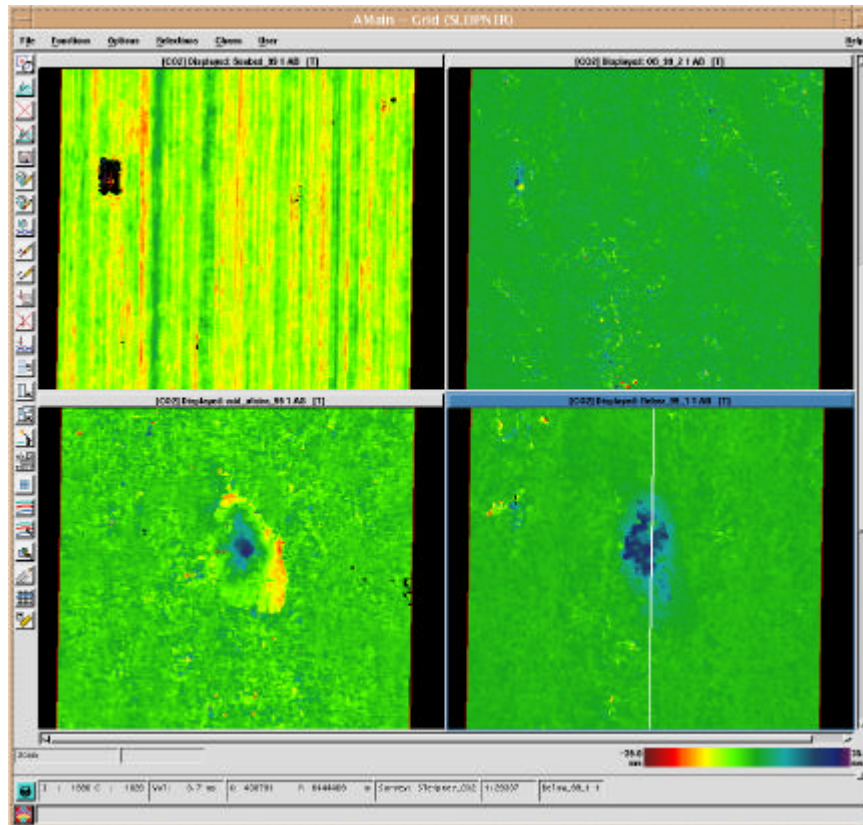

Figure 1. Time difference for reflectors between the 99 survey and the 94 survey. *Upper left corner*: Seabed. *Upper right corner*: Reflector 200 ms above Top Utsira. *Lower left corner*: In the middle of the Utsira Formation. *Lower right corner*: Reflector 200ms below Base Utsira.

In the middle of the Utsira Formation, large time differences between the two surveys may be observed around the injection point. The time shifts are both positive and negative, in the range of +/-25ms. A pull-down effect is observed at the base of the Utsira Formation, proving that the seismic wave field experiences a substantial velocity reduction when travelling through the CO_2 cloud. At the edges of the cloud, pull-up effects are observed, introducing a parabola-like reflector geometry. The reason for the pull-up are most likely due to effects introduced by the pre-stack time migration that was performed in the prior processing sequence of the seismic data. This effect is illustrated in Figure 2.
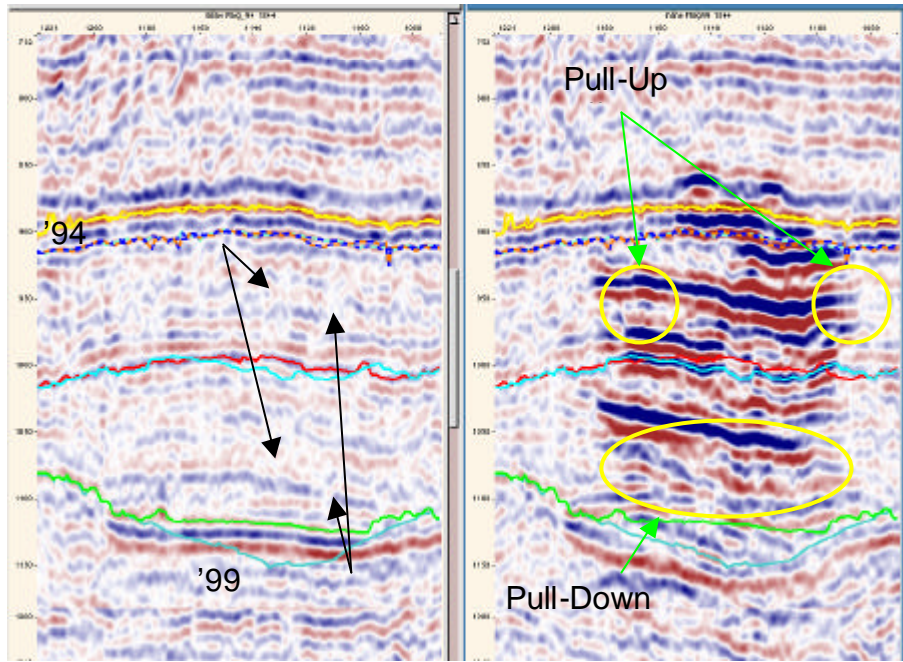
Figure 2. Illustration of "pull-up" and "pull-down" effects in CO_2 cloud. The '94 data is shown to the left, whereas the '99 data is shown to the right.

Some differences have been observed between the two surveys that may be related to small differences in processing between them. This is exemplified in Figure 3, where vertical striping effects have been observed on the '94 seismic data. This "noise" results in less continuous reflectors, and makes the interpretation less accurate. Compensation for this could be done by post-processing the '94 seismic data with filters that enhance lateral continuity.
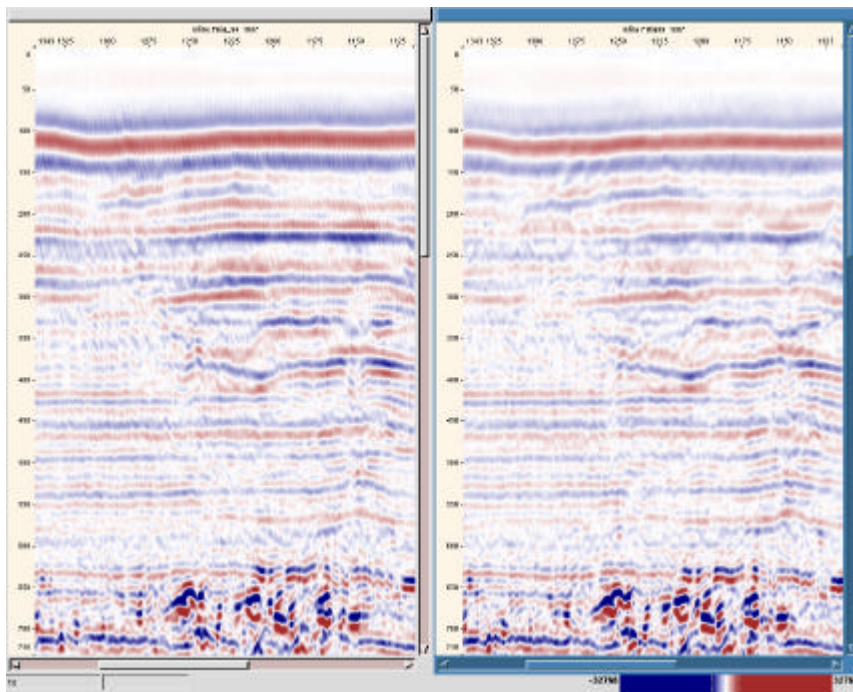

Figure 3. *Left panel*: 94 final migrated seismic from seabed with vertical striping. *Right panel*: 99 final migrated seismic.

Wavelet-based repeatability analysis

Another measure of repeatability is derived from the wavelets of the different seismic surveys. Difference in the seismic wavelet phase outside the CO_2 affected area may be an indicator of lack of repeatability. However, small phase differences are only detected by a combined estimation of the wavelets, and hence we have developed the 4D blind deconvolution technique. First, 4D Blind Deconvolution (4DBD) is applied to two different seismic cubes (the 1994 cube and either of the time-lapse cubes, for instance). The 4DBD routine assumes that the reflectivity is constant and outputs an estimate of a common reflectivity cube for the two input cubes. One wavelet cube and one global wavelet are also estimated for each cube. The principles of the 4DBD technique are illustrated in Figure 4 and Figure 5.
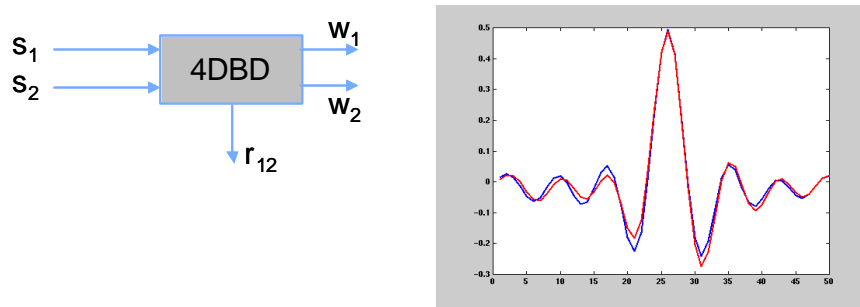

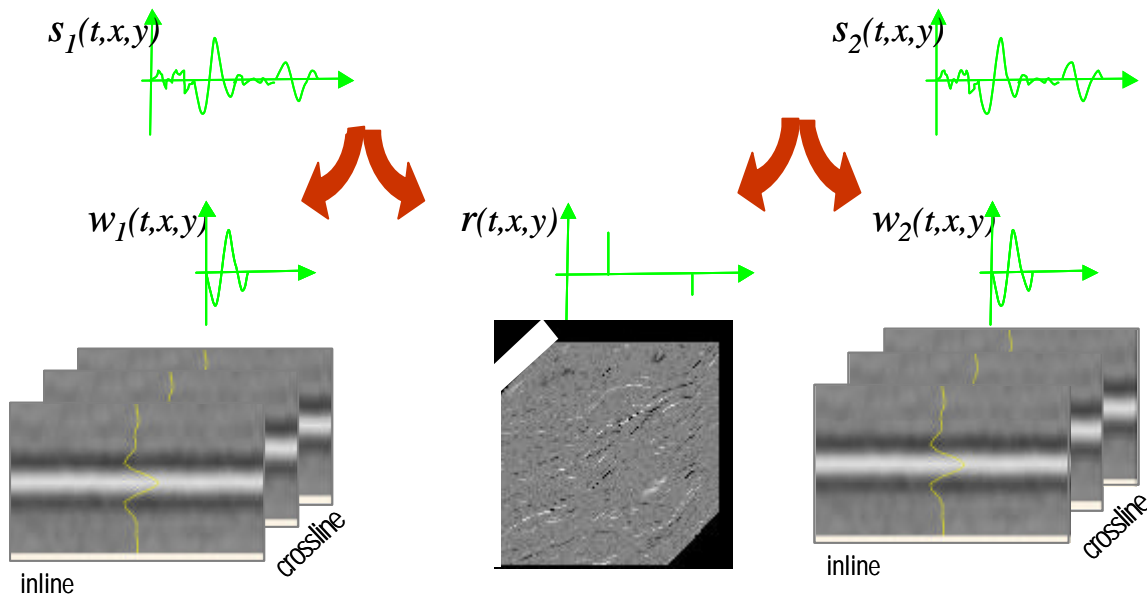Figure 4 4D blind deconvolution principle (1:2).

Figure 5 4D blind deconvolution principle (2:2).

Next, when the wavelets are known, the mean frequencies for the wavelets are computed, as illustrated in Figure 6. Changes in mean are then found by differencing the result and the results are shown in Figure 7. Another measure capturing the repeatability is the scaling factor, i.e. the ratio between the different wavelets. This measure is illustrated in Figure 8.

$$w(t) \quad \underset{FFT}{\Longrightarrow} \quad W(f)$$
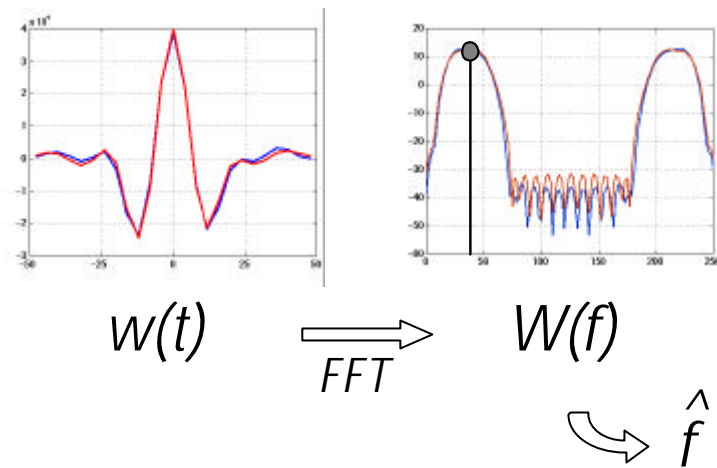
$$\hookrightarrow \hat{f}$$

Figure 6 Computation of the mean frequency of an extracted wavelet. The central frequency is estimated as the peak of the Fourier magnitude spectrum.

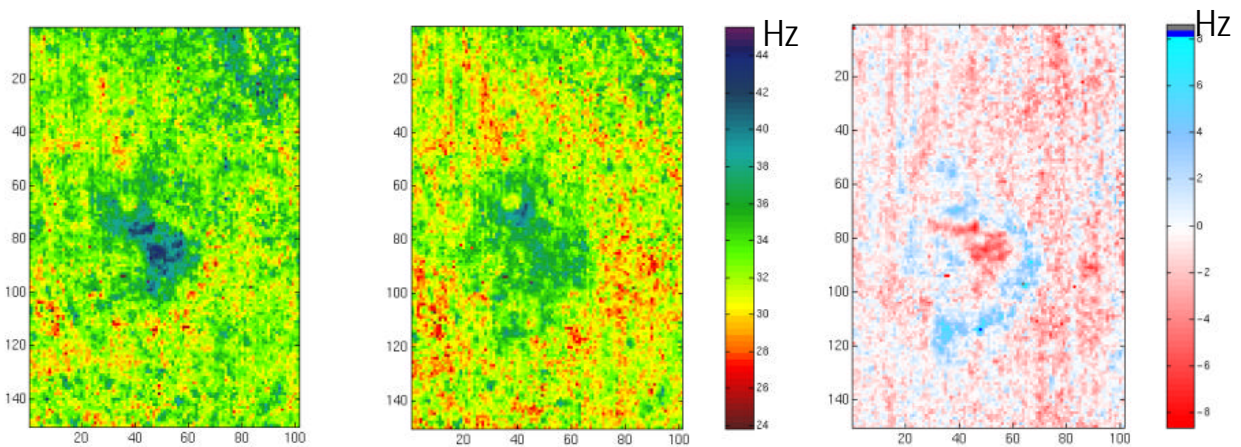Mean frequency 99   Mean frequency 01   Difference

Figure 7 The mean wavelet frequencies of the 1999 and 2001 seismic cubes and their difference. A small absolute difference (white) indicates good repeatability.
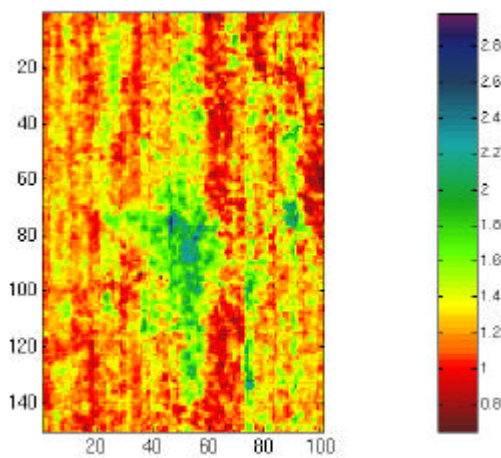

Figure 8 The scaling factor; the ratio between the wavelet energies from the 1999 and 2001 seismic. A scaling factor of 1 (red) indicates good repeatability.

Seismic mapping and characterisation of CO2

Introduction

Seismic time-lapse mapping and characterisation of CO_2 in the Utsira Sand is performed with use of different attribute techniques. Available seismic time-lapse data sets from 1994, 1999 and 2001 are used from the SACS survey.

In the CO_2 injection area, the Utsira Sand is about 200m thick and consists mostly of Miocene turbidite sand, partly separated by thin shale layers (approx. 1m). The intra shale layers in the Utsira Sand are represented by relatively poor seismic quality in the 1994 data (pre- CO_2 injection) (Figure 9). Reflections are partly discontinuous, chaotic and often disturbed by underlying shadows from amplitude anomalies in the overburden (Pliocene sediments).

As a result of the CO_2 injection, several strong reflections appear, and are a result of increased acoustic impedance contrast between thin shale layers and CO_2 filled sand (Figure 10). These shale layers are partly sealing the CO_2. The CO_2 injection causes also a pull-down effect that increase with depth as a result of distance of CO_2 filled sand that the P-wave travels in. A thin shale layer of approx. 5m thickness separates an approx. 25m thick sand wedge layer from the Utsira Sand underneath (Figure 9). Amplitude anomalies indicate CO_2 leakage into the sand wedge layer in both the 1999 and 2001 data (Figure 10). Thick Pliocene shale packages above are supposed to seal further leakage.
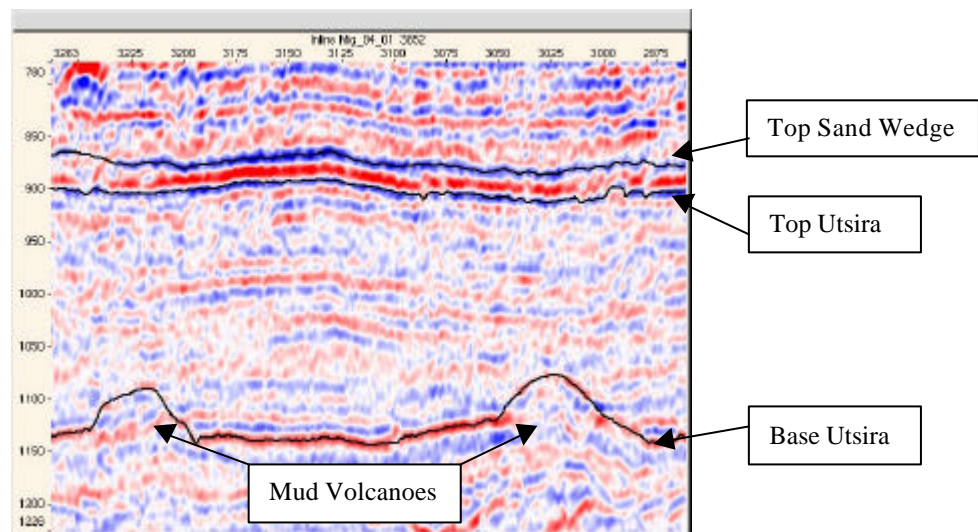

Figure 9 Utsira Sand in the CO_2 injection area, defined between the Top- and Base Utsira horizon. The seismic reflection signals in the Utsira Sand have relatively poor quality. An approx. 25m thick sand wedge layer lies above the Utsira Sand, separated by an approx. 5m thick shale layer. The Base Utsira horizon reflects the underlying mud volcanoes.
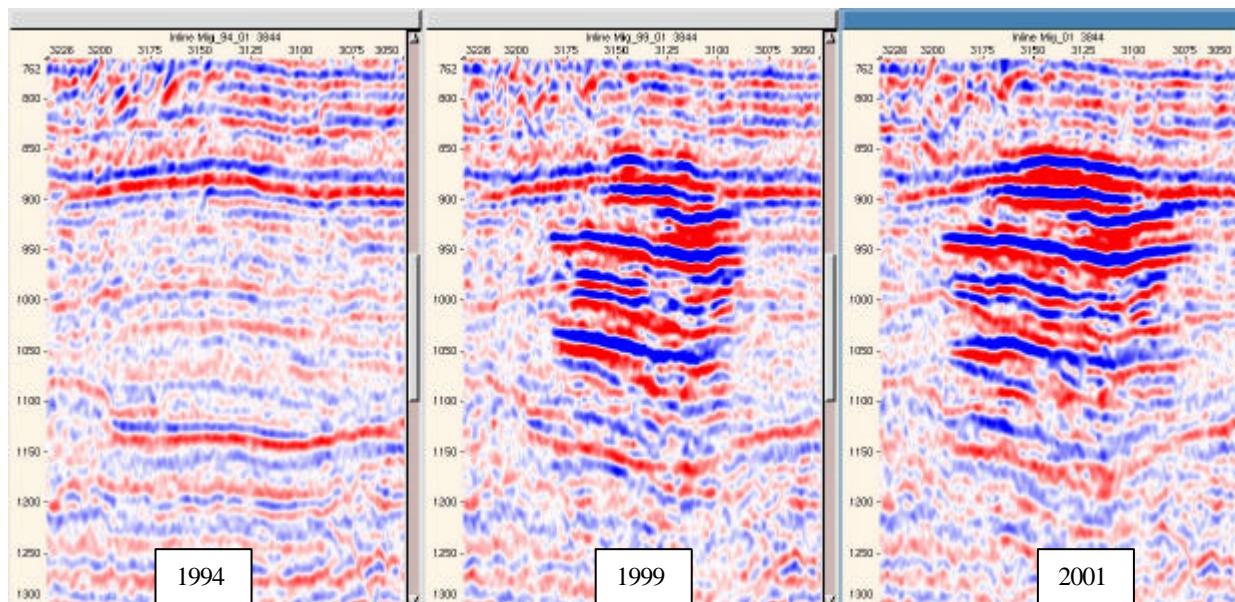
Figure 10 The injected CO_2 is clearly visible in the time-lapse data due to increased impedance contrast between thin shale layers and CO_2 filled sand. Strong pull-down effect is obvious in the middle and lower parts of the Utsira Sand.

Objective

The focus in this work has been to perform an as detailed mapping and characterisation of the CO_2 as possible, with use of seismic data. In addition to standard Charisma interpretation and visualisation tools, different attributes are used. This includes 3D Spectral Energy Difference (SED) cubes for mapping the top of the CO_2 accumulations and characterisation of the CO_2 flow inside the reservoir, 3D Extrema classification for mapping the top of a thin intra-reservoir shale layer which defines a poor reflection in the 1994 base survey, and Non Rigid Matching (NRM) which gives a continuous 3D pull-down estimate between the 1999 and 2001 data.

Geometry of the Utsira Sand in the CO₂ injection area

The geometry of Utsira Sand is strongly affected by compaction of underlying mud volcanoes (/diapirs) (Figure 9). The Utsira Sand and parts of the overburden shows depressions and syncline geometry above the volcanoes, while intervening areas stand out as domes and anticlines. The top and base horizon of the Utsira Sand reflects this geometry (Figure 11). Around the injection point, the Top Utsira Sand defines partly a dome shape and partly a NE striking anticline shape, which serve as a structural closure to the CO_2.

Mapping of CO₂ sealing shale layers

The SED cube was used to map the thin CO_2 sealing shale layers in the 1999 and 2001 data, which also represent top of the CO_2 accumulations (Figure 12). To map the CO_2 in 1999, the SED was computed with the 1994 and 1999 seismic data as input. In the same way, CO_2 was mapped in 2001 with the 1994 and 2001 seismic as input. The resulting SED cubes made it easy to do auto-tracking with a suitable "energy-difference" threshold value as parameter setting. It also simplified the more detailed part of the mapping, compared to interpretation from the original seismic cubes.
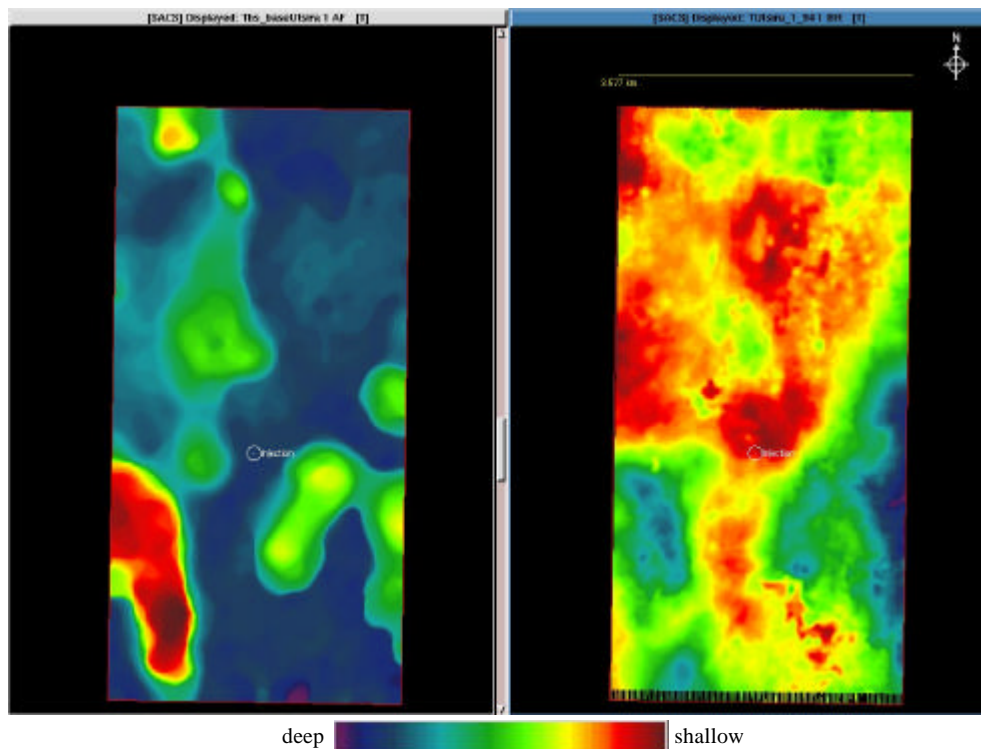
deep [colour scale] shallow

Figure 11 Top Utsira- (right) and Base Utsira horizon (left). The Base horizon reflects the underlying mud volcanoes. Compactions of these volcanoes have strongly affected the geometry of the Utsira Sand, characterised by depressions, domes and anticlines. Note the inverse similarity in geometry between Top and Base Utsira horizon.

In total, 9 CO_2 sealing shale layers where mapped from the 1999 data and 10 were mapped from the 2001 data, including leakage into the Sand wedge (Figure 13). This means that the CO_2 was trapped in one new location in 2001 compared to 1999. All the same layers in the 1999 data shows an extension of CO_2 sealing in the 2001 data. Extension of the CO_2 is also obvious when looking on the seismic sections (Figure 10). From Figure 13 it's evident that the CO_2 layers shows an increasing pull-down effect deeper and towards the central area, close to the injection point.

Mapping of an intra shale layer using 3D extrema classification

One of the intra-reservoir shales where mapped from the 1994 seismic data (pre-injection). The reflection is interpreted to correspond to the largest CO_2 sealing layer observed from the 1999 and the 2001 data (Figure 13). Since the seismic quality in the injection area is relatively poor, 3D interpretation of this reflection signal was performed with use of an extrema classification cube (Figure 14).

The extrema classification cube is obtained by classifying the seismic attributes only along minimum and maximum values in the original seismic cube. A number of attribute values are chosen, but only their values at the extrema positions are included in the classification. This classification distributes the seismic events into classes of similar attribute response along the minimum/maximum value of the seismic signal, and can be applied in the structural interpretation of the seismic cube. The volume classified was defined from above the sand wedge layer, down to the deepest half of Utsira Sand. The area classified covers the lateral distribution of all CO_2 in 2001.
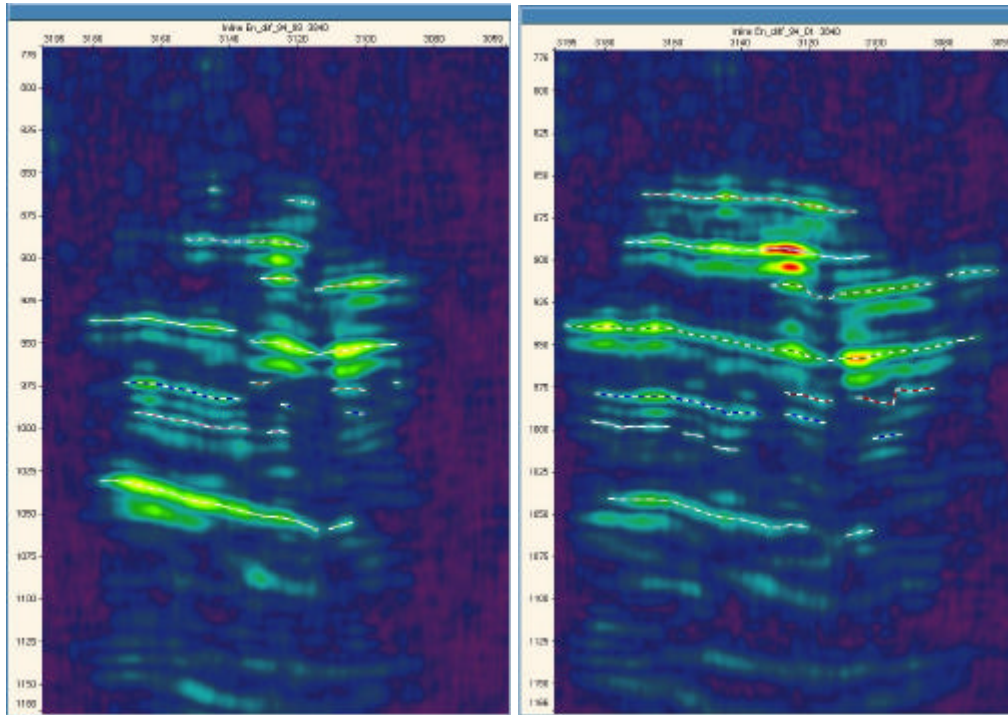
Figure 12 Top of the CO$_2$ accumulations (base of thin shale layers) in 1999 (left) and 2001 (right) where mapped from SED cubes.
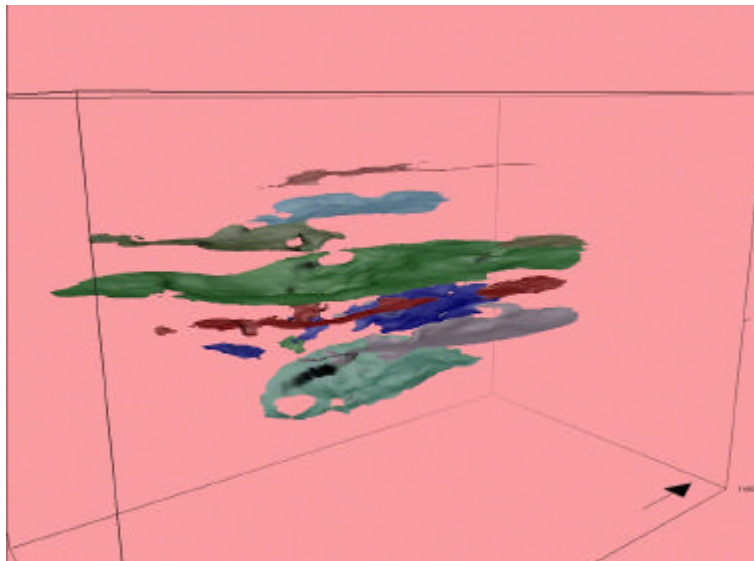

Figure 13 Visualisation of the CO$_2$ sealing layers including the Top Sand wedge. Note the increased pull-down with depth in the central parts.

Interpretation of the intra shale layer was done in two iterations. First, manual drawing of the horizon (line by line) in inline and crossline direction was performed on the class believed to represent the shale layer (the original seismic cube was hidden away while interpreting). Second, the manually interpreted horizon was used to guide an extrema-class consistent horizon picking of the respective class. A structural editor tool was used to pick out the resulting horizon. If the extrema-class points was at, or closer than 8ms to the manual interpreted horizon, the points where added to define the new class consistent horizon.

Figure 15 shows the result of the extrema class consistent horizon that represent top of the intra shale layer. This shows that the layer reflection is most continuous in the southern part, and in the NE corner of the

classified area. When gaps are interpolated, the horizon shows similar geometry as the Top Utsira horizon (Figure 15). This result should be expected and give confidence to the intra shale interpretation.

For a spatial comparison of this interpolated horizon with the pull-down affected 1999 and 2001 interpretations, a subtraction map (or thickness map) was made. If the edges of the 1999 and 2001 horizons show a close match to this 1994 horizon, where the pull-down values are expected to be low, it is very likely that the 1994 shale layer interpretation is correct. The result of this, shown in Figure 16, illustrates that the westernmost edge of the time-lapse interpreted horizons lies above the 1994 horizon, while the easternmost edge lies below. Still, the offset is never more than about 10ms up and down.
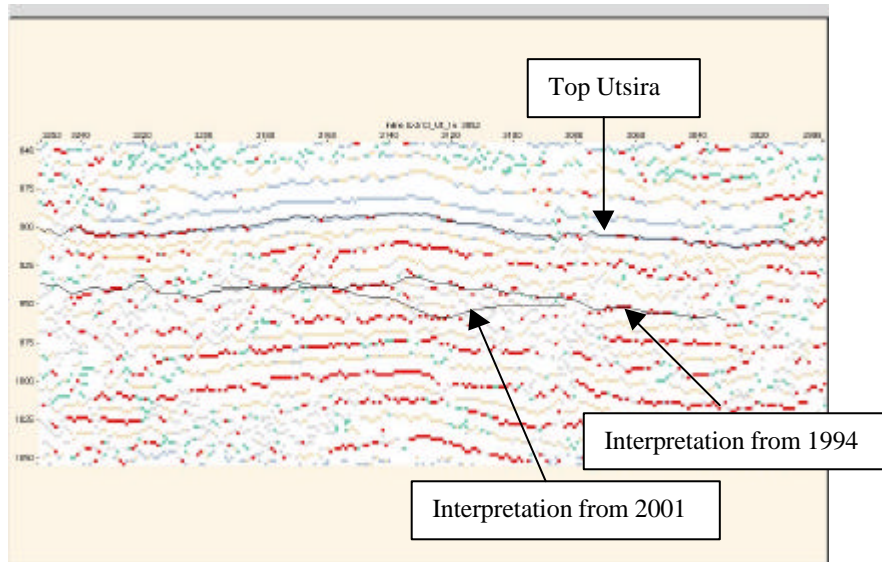

Figure 14 Extrema classification cube is used to map one of the CO_2 sealing shale layers from the 1994 data, following a red class. Red class may in general represent top of all the intra reservoir shales. Note that open gaps in the 1994 intra shale horizon are here interpolated.
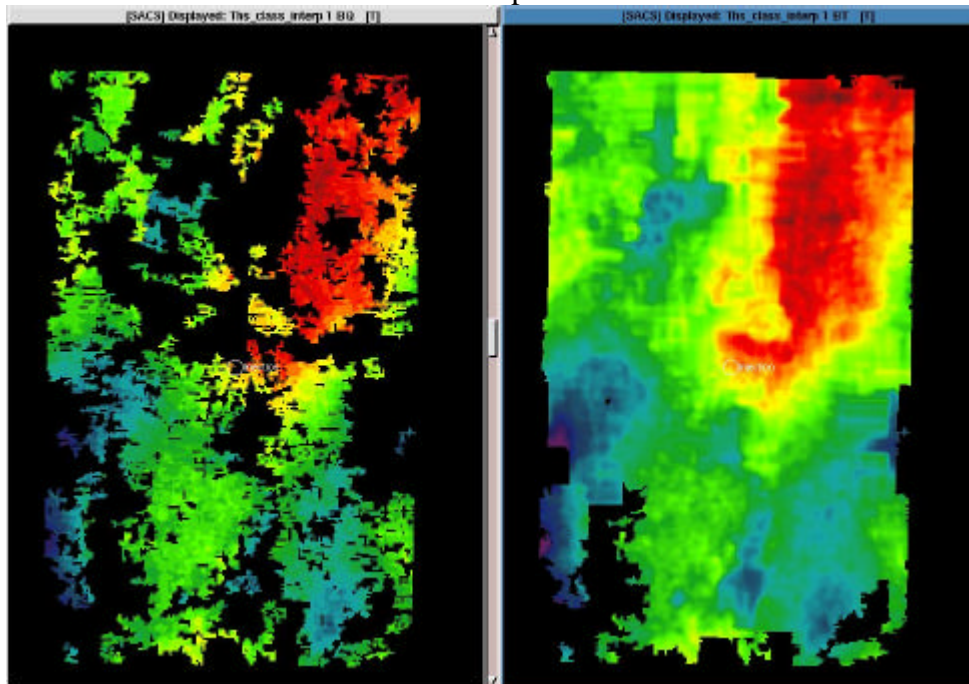

Figure 15 Extrema class consistent horizon interpretation of the intra shale layer (left). Intra shale horizon with interpolation of the gaps (right).
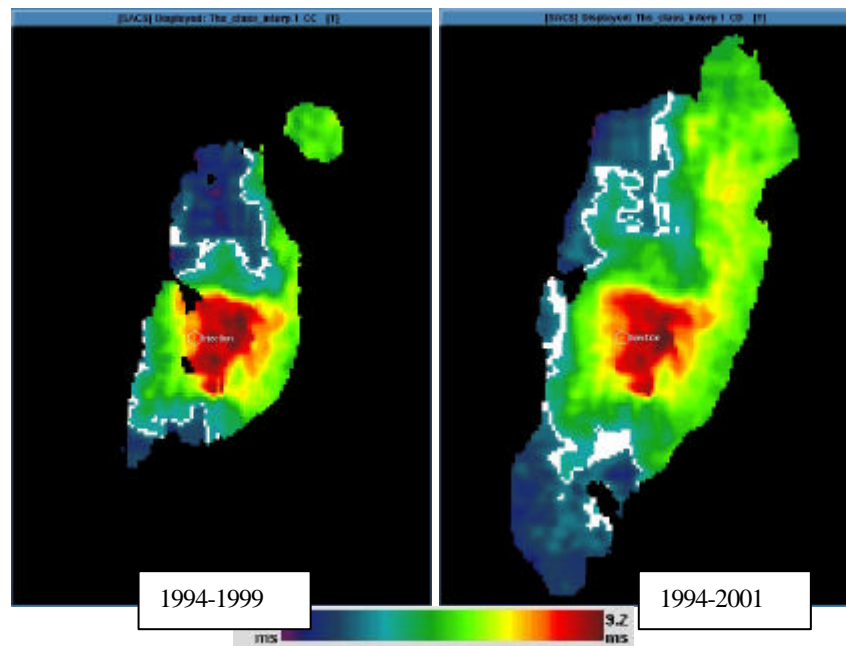
Figure 16 Subtraction of the 1994 interpretation with the 1999 horizon (left) and the 2001 horizon (right). The white contour indicates intersection between the horizons (or zero value).

Detailed seismic characterisation of the CO$_2$

Grid-based SED volume attributes was made to investigate each of the CO$_2$ sealing layers in a map view. The volume windows follow the geometry of the respective layers that they capture with a vertical size of 12ms. The resulting maps show energy-difference that can directly be related to the CO$_2$ flow.

From the largest CO$_2$ sealing layer, Figure 17 shows the distribution of energy-difference in 1999 and 2001, compared to 1994. In both cases, it is clear that the CO$_2$ distribution is mainly controlled by the structural closure of the shale layers. In addition, several internal linear structures can be observed, especially from the 2001 distribution. The most evident ones are striking NW-SE and NNW-SSE (Figure 17). Also, the eastern and western CO$_2$ boundary defines distinct NNE-SSW striking lineaments. All the lineaments are believed to represent flow boundaries. These flow boundaries may be stratigraphic related or related to faults.

Motivated by the positions of these lineaments, manual fault interpretation was carefully done in the 1994 seismic data (Figure 18 and Figure 19). In the seismic data, 6 discontinuities characterised by vertical offset and/or flexure of the layer reflections, was identified as normal faults (Figure 19). Since the vertical seismic resolution of the data is poor and the fact that some identified faults have offset close to the resolution limit, the interpretation contain some degree of uncertainty. The criteria for identify each of the faults was that they could be interpreted over a certain vertical and horizontal distance by drawing fault cuts in several inlines and/or crosslines (Figure 18). Figure 20 illustrate the "energy-difference distribution" of the main CO$_2$ accumulations including the CO$_2$ leakage in the sand wedge. The trace where the faults cut each of the CO$_2$ levels is displayed. Notice fault 2 (red) that separates two domains of high energy-difference values from the Top Sand wedge and Top Utsira levels. Fault 3 (blue) seems to act as a flow boundary in the Top Sand wedge and level 10. Fault 5 and 6 (mauve) is clearly defining a flow boundary in the Top Sand wedge level and seems also to partly affect level 8 and 10. Fault 3 and 4 do not represent any obvious flow boundaries, except from level 5 (largest CO$_2$ accumulation). The fact that the manually interpreted faults partly seem to define flow boundaries in the other CO$_2$ levels gives confidence that at least some of the observed flow boundaries represent faults.
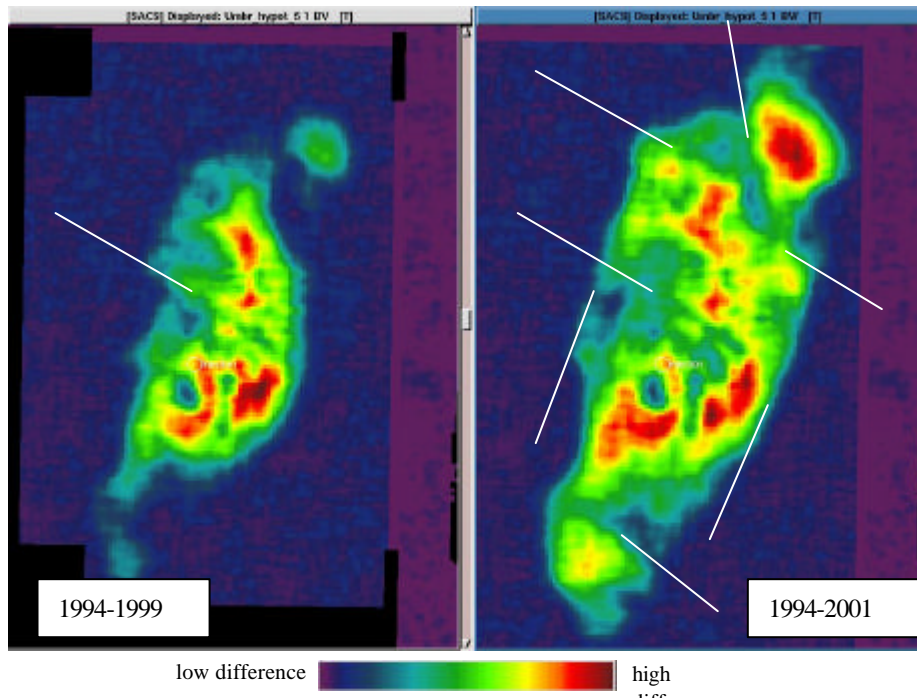
Figure 17 Energy-difference distribution in the 1999- and 2001 data, compared to the 1994 data. Linear structures are evident from this distribution, especially from the 1994-2001 difference. The lineaments are interpreted to represent flow boundaries. White lines indicate the position of the lineaments.
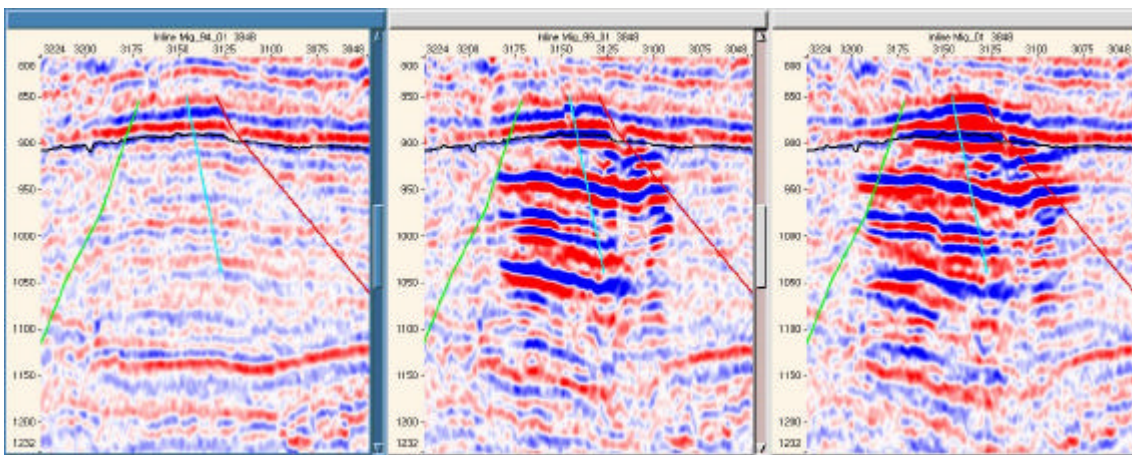

Figure 18 Manual fault interpretation in the 1994 data (left) by drawing fault cuts. The faults are displayed upon the 1999 data (middle) and 2001 data (right).
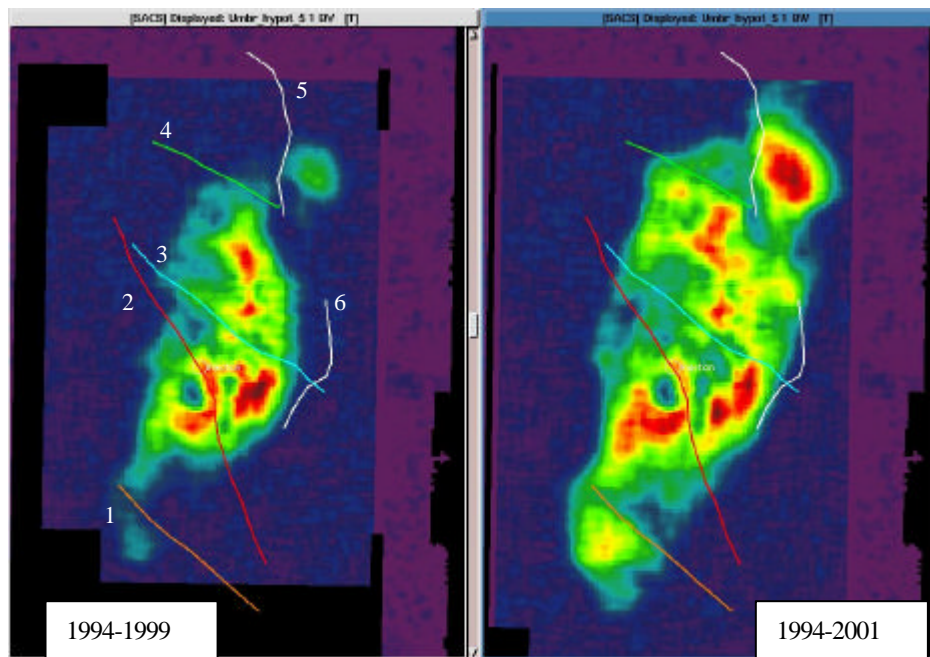
Figure 19 Guided by the flow boundaries observed from the SED maps, 6 faults where interpreted. The faults are numbered 1-6.
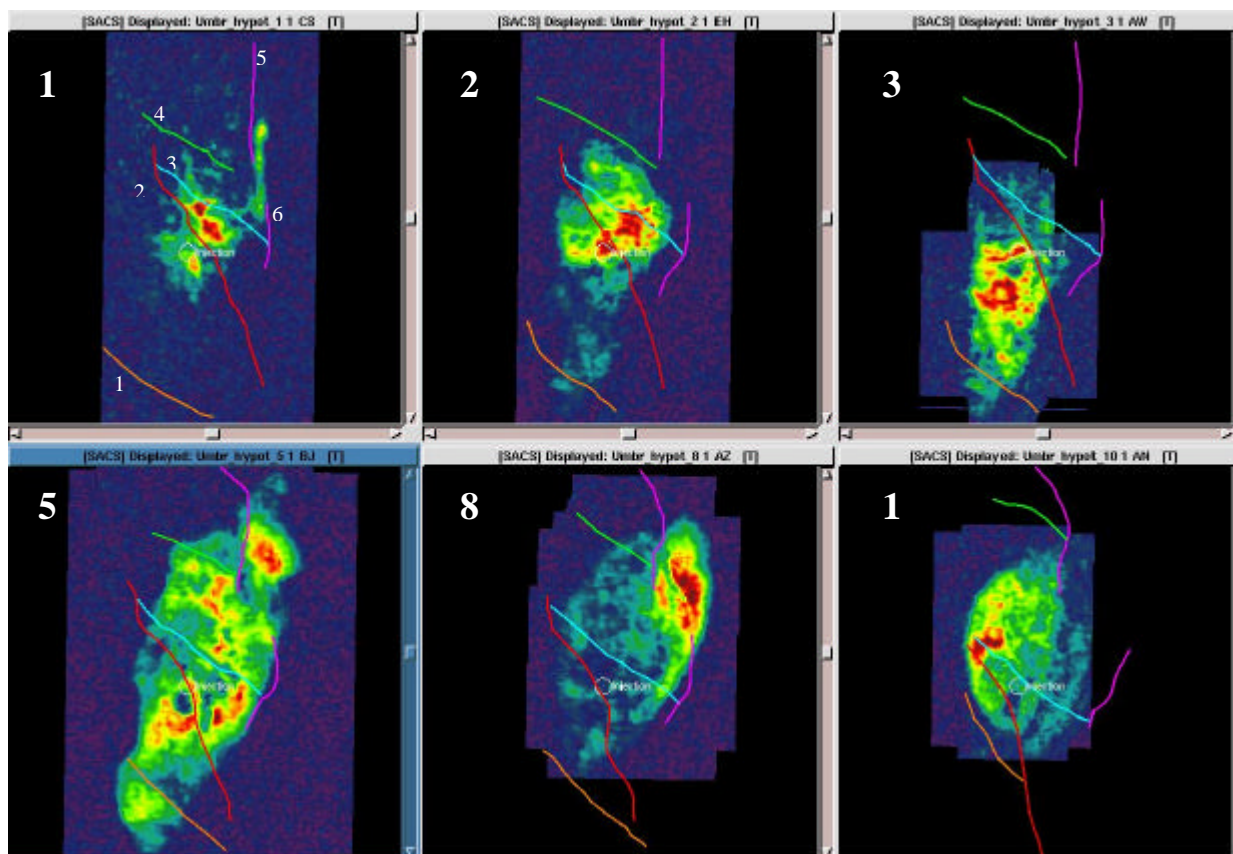
Figure 20 Energy-difference (1994-2001) from the main CO_2 accumulations including the Top Sand Wedge (level 1) down to the deepest CO_2 sealing shale (level 10). Each of the CO_2 accumulations are numbered in levels according to their depth position.

The intra shale layer horizon, interpreted from the extrema-classification cube, shows a clear NW-SE striking boundary, located in the area between fault 2 and 3 (Figure 21). This boundary is suspected to represent a fault as well. When this boundary is displayed upon the energy-difference from 2001 (Figure

21), it seems to represent a flow boundary, striking in an oblique direction compared to fault 2 and 3. It's hard to observe this fault (fault 7) in the 1994 seismic data, but it may exist because reflections are quite poor with low continuity in this area. When fault 2 and 3 are compared to the intra shale horizon, they are positioned mostly in areas where the intra shale lacks a reflection signal, and are therefore not standing out as visible boundaries. On the other hand, fault 5 seems to match a N-S striking boundary.

A partly continuous gap, with a N-S orientation, is observed from the southern-central part of the intra shale horizon (Figure 21). This gap is suggested to represent a channel because of its meandering shape. If this assumption is correct, sand is cutting the shale layer, which results in a lack of reflection. A channel like this can explain some the CO_2 flow pattern. In Figure 21, the interpreted channel trace is displayed upon the "energy difference" map. From this comparison, it is obvious that the channel follows low energy-difference values that could be expected due to the lack of the shale reflection. The interpretation of the channel is still speculative since this it's not clearly observed from the seismic data.
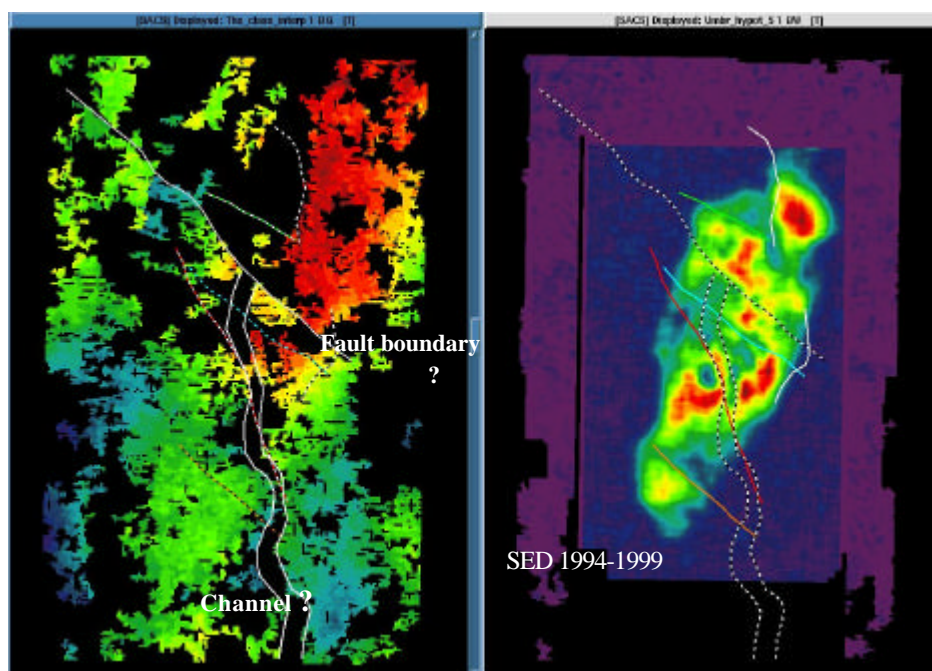

Figure 21 A sharp NW-SE striking boundary is obvious from the intra shale horizon (left). In the southern part, a continuous N-S oriented gap in the horizon may indicate a channel structure. Comparison of the SED map with fault interpretation is shown to the right. It looks like the horizon boundary matches with a CO_2 flow boundary.

Automatic pull-down estimation

3D automatic estimation of CO_2 related pull-down between the 1999 and 2001 data was performed using Non Rigid Matching (NRM). The resulting pull-down cube can be related to the 3D distribution of the stored amount of CO_2 in this period (Figure 22). Figure 23 illustrate a map view of pull-down around the largest CO_2 accumulation (CO_2 level 5), compared to a subtraction map between the 1999 and 2001 horizon, which also gives a pull-down estimate for this level. It's clear that areas with the greatest pull-down values matches between the two maps. This suggests that the automatic method gives good quality estimates.
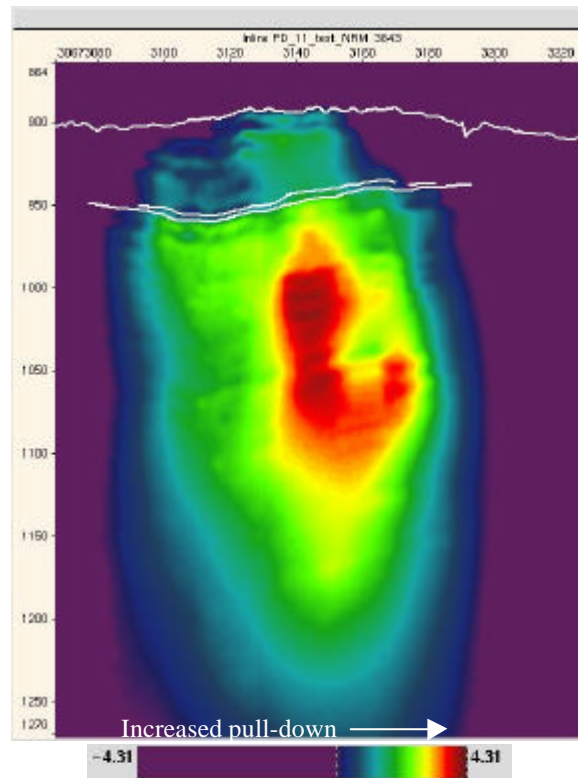
Figure 22 NRM pull-down estimation (vertical section). The 1999 and 2001 horizon of the largest CO_2 layer is displayed together with Top Utsira (at the top).
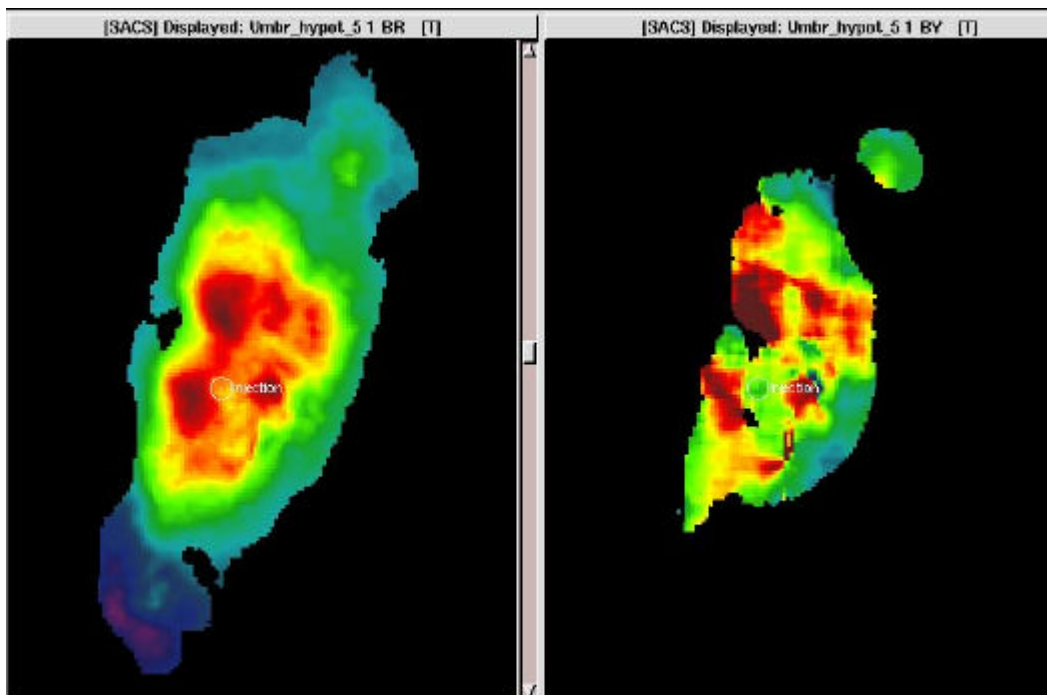

Figure 23 Pull-down map from the NRM cube around the largest CO_2 layer (left). Pull-down estimated by subtraction of the 1999 horizon from the 2001 horizon of the CO_2 layer.

Overburden analysis

Introduction

Amplitude anomalies are observed in the Pliocene sediments (Upper and Lower) on top of the Utsira Sand (Figure 24). Some are also observed along the Top Utsira reflection. The anomalies show strong negative impedance contrast and are believed to represent old gas accumulations, widely distributed in the ST98M11 survey area. A natural question to ask is whether this gas has leaked up from the Sleipner gas reservoir deeper down, or if its source rock is in the overburden. If the gas has migrated from the Sleipner gas reservoir, potentially leakage paths may be above the strongly compacted mud volcanoes(/diapirs) (Figure 25). Strong compaction may have induced fractures in the shale-rich Pliocene sediments and enhanced it's permeability (Figure 26).
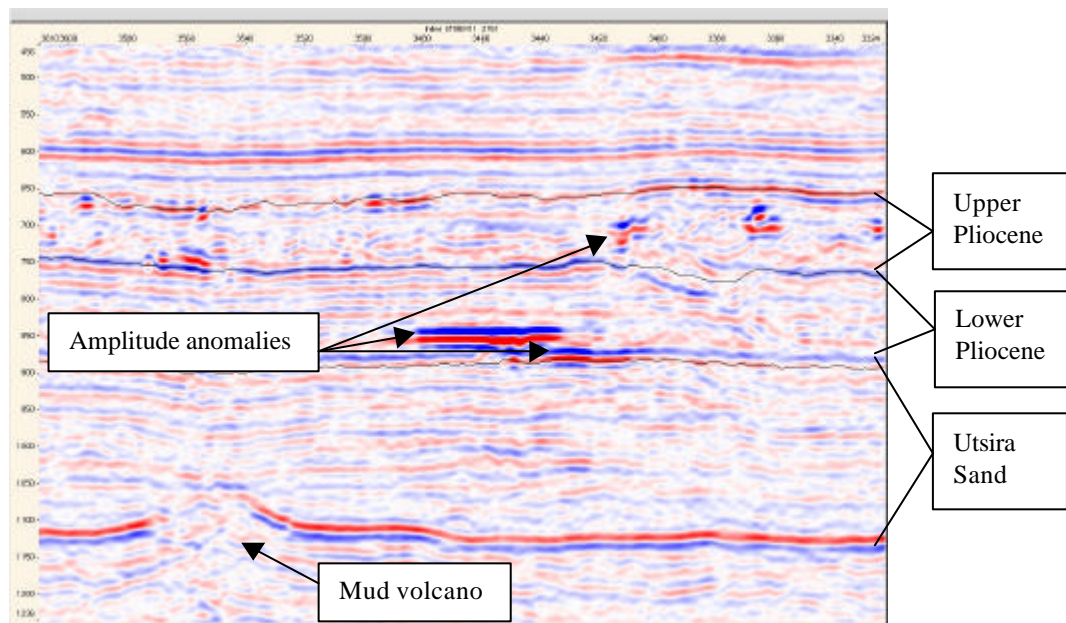

Figure 24 Amplitude anomalies distributed in the Upper- and Lower Pliocene sediments, and at the top of Utsira Sand.

The Upper Pliocene sediments show an increased thickness in the central north-eastern area which is interpreted to be glacial depositions. NE-SW striking lineaments are interpreted as glacial plough marks. The gas distribution, indicated by the amplitude anomalies, seems partly to follow these structures.

Objective

The focus of the overburden analysis has been to map the distribution of gas in the entire ST98M11 survey area. If the gas accumulations that are trapped in different layers show some degree of vertical spatial correlation with each other, and with the underlying mud volcano positions, gas leakage caused by mud volcano compaction is likely. Unsupervised grid-based classification is used as to map the gas. Classification maps make clear images of the gas distribution and comparison of the gas positions between the different layers are easy.
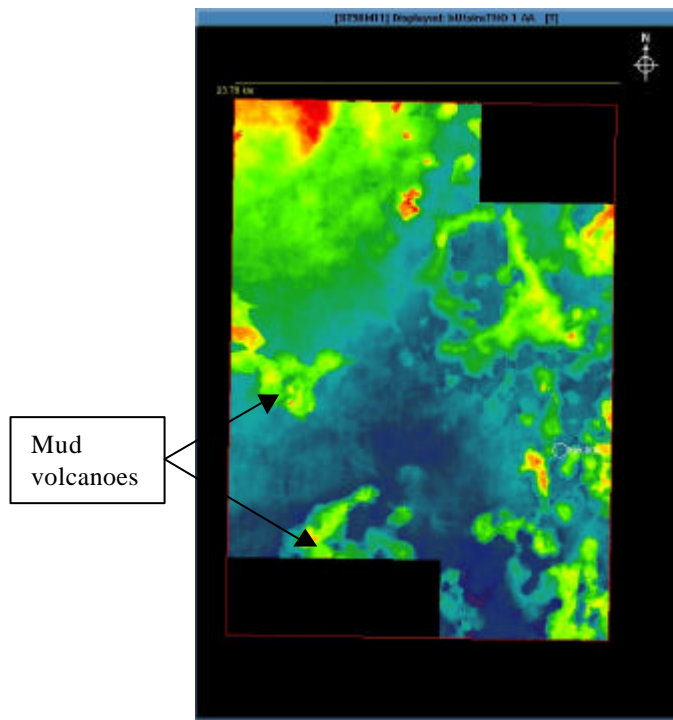
Figure 25 Time map horizon of Base Utsira illustrating the distribution of mud volcanoes. The horizon map shows the extension of the ST98M11 survey area. The north direction is indicated by an arrow.
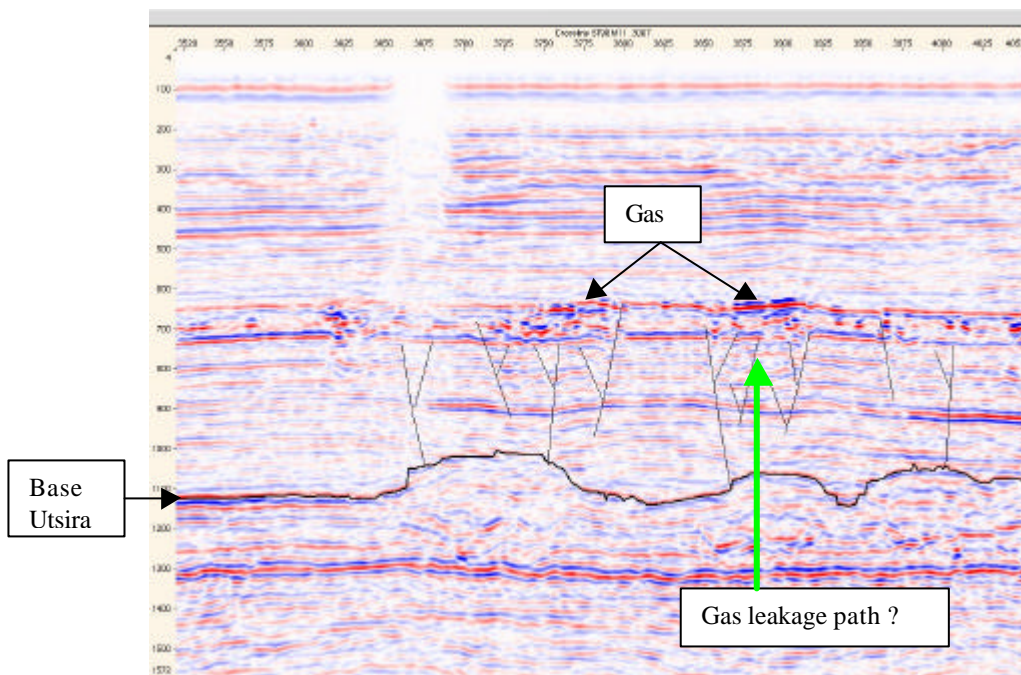
Figure 26 The Utsira Sand and the Pliocene sediments show depressions above the mud volcanoes. Faults may have been generated and caused gas leakage into the overburden. Base Utsira indicate the top of the mud volcanoes.

In addition to map the gas distributions in a map view, 3D extrema classification is used for geometrical characterisation of the gas containing sediments in the central-north-eastern area. This technique simplifies mapping of 3D sediment bodies, which is important regarding gas migration paths and distribution within the Upper Pliocene sediments.

Geometry of the Upper Pliocene sediments – Top and Base horizon

Horizon interpretation of Top Upper Pliocene and Base Upper Pliocene, which defines the top and base of the Upper Pliocene sediments, are shown in Figure 27. Both horizons have an overall dip to the SW and show a NE-SW trending depression in the central part of the ST98M11 survey area. The base horizon reflects a very distinct NE-SW and ENE-WSW striking lineament pattern. In a seismic cross-section (Figure 28), these lineaments often appears as well-defined through shapes and are most possibly representing glacial plough marks. A relief map of the base horizon from the SACS survey area is shown in Figure 28. This map gives a closer and more detailed image of the plough marks and clearly demonstrate their through shape. It is also visible that some of the plough marks are oriented more to the N-S compared to the general NE-SW trend

A thickness map measured in time was made by subtracting the base horizon from the top horizon (Figure 29). The lineament pattern is again very obvious, representing thicker volumes above the plough marks. In addition, pronounced thickening of the sediments are evident from the central part to the northeastern part of the survey area. The shape of the thickened area is clearly affected by the lineaments which here shows an ENE-WSW orientation, compared to the general NE-SW orientation for the rest of the area.
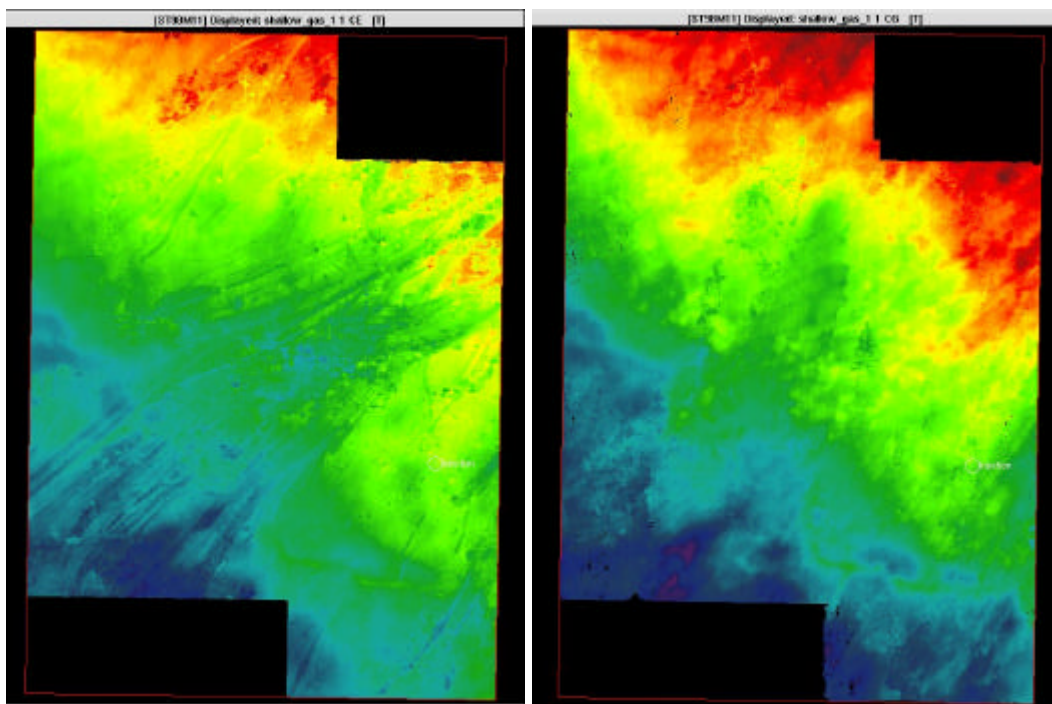
Figure 27 Horizon time maps showing the top (right) and base (left) of the Upper Pliocene sediments.
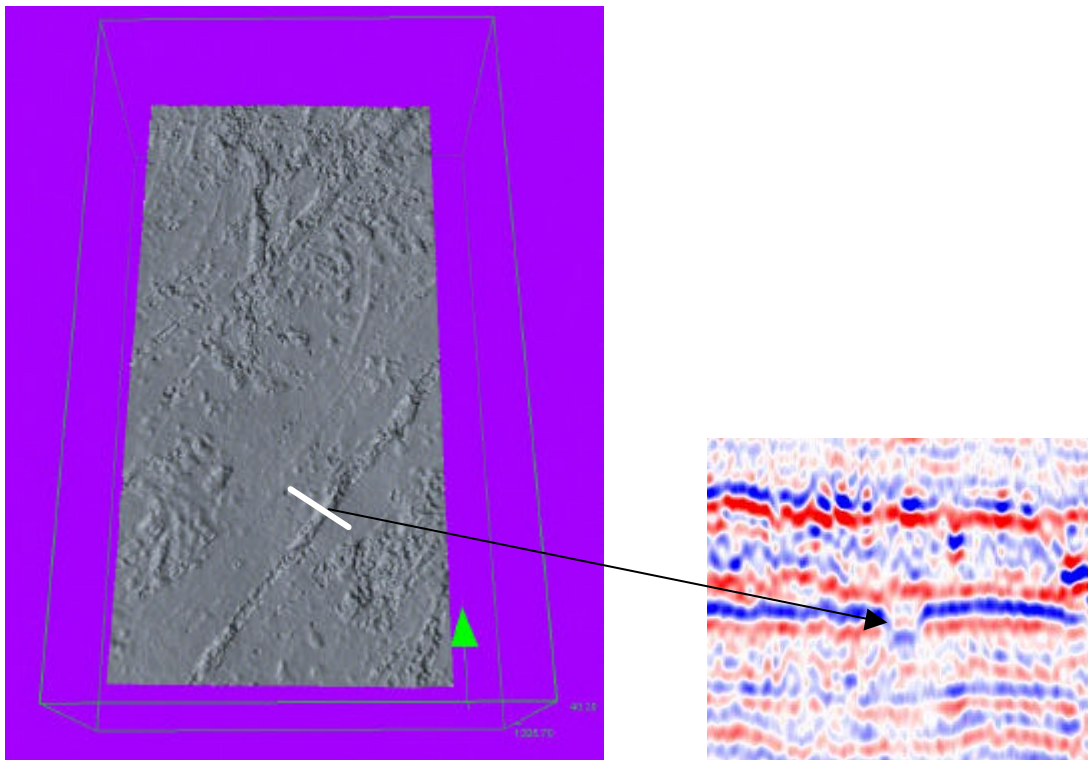
Figure 28 NE-SW and N-S striking plough marks are clearly visible from a relief image of the Base Upper Pliocene horizon (left). The horizon extension is defined by the SACS survey. In a cross-section (right), the plough marks shows an obvious trough shape.

Figure 29 A vertical time thickness map made by subtraction of Base Upper Pliocene from Top Upper Pliocene. Note the thickened areas in the central to the northeastern part.

Geometry of the Upper Pliocene sediments – Distribution of amplitudes

The Integrated Amplitude attribute was calculated from a Gaussian low-pass filtered cube. This attribute gives a nice image of the amplitude anomaly distribution in the Upper Pliocene se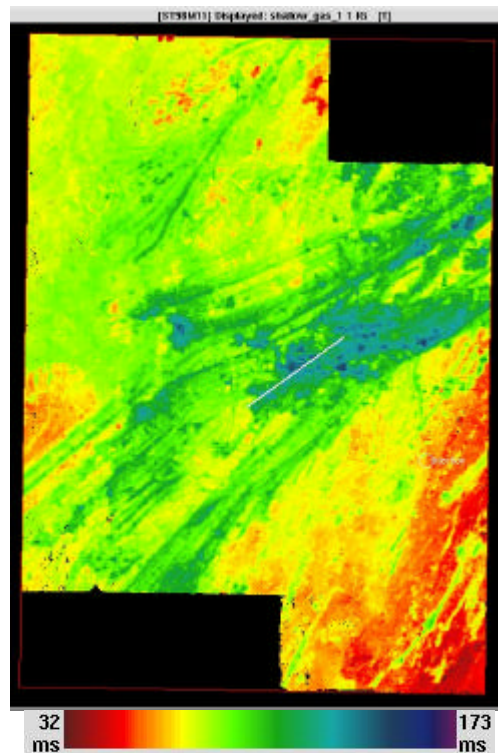diments. The anomaly distribution reflects most possibly the gas distribution, but is also affected by thickness variation since the attribute was calculated between the top and base horizon. Figure 30 shows that the amplitudes highlights the plough marks and the thickened areas. The deviation in plough mark orientation from the general NE-SW to ENE-WSW in the thickened area is obvious. Also, the amplitude distribution in the centre of the thickened area seems to define internal tapering curved geometries towards SW. In a seismic cross-section oriented NW-SW, the thickened area defines several mounded shapes which seems to continue as ridges (Figure 31). This, together with the deviation in plough mark orientation, makes interpretation of these observations as an end moraine complex likely.
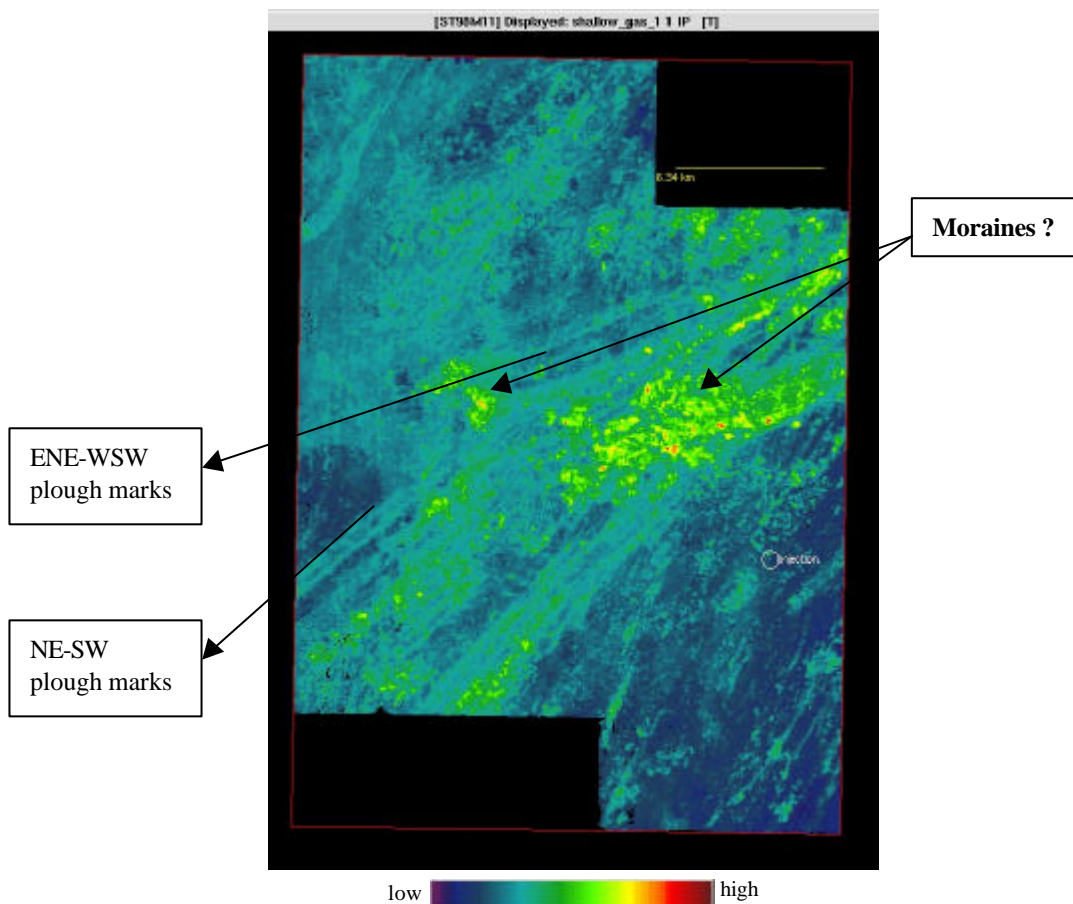
Figure 30 Integrated amplitude from a gaussian filtered cube. The amplitude distribution highlights both NE-SW striking plough marks and possible moraine structures in the thickened area. Note the deviation in plough mark orientation from NE-SW to NNE-SSW in the thickened area.

In the uppermost part of the Upper Pliocene sediments, the integrated amplitude attribute is calculated with a constant window of 40ms (no thickness effect). The resulting amplitude map (Figure 32) displays NNE-SSW trending structures in the central and the northeast part of the survey area. The structures show a slightly meandering shape and are interpreted to represent channels. A closer image of these channel structures reveals an obvious meandering shape (Figure 32).

Figure 31 A seismic cross-section illustrating possible moraine ridges in the thickened area.

Figure 32 Integrated amplitude from a gaussian filtered cube of the uppermost part of the Upper Pliocene Sediments. The map illustrates possible NNE-SSW oriented channel structures in the central a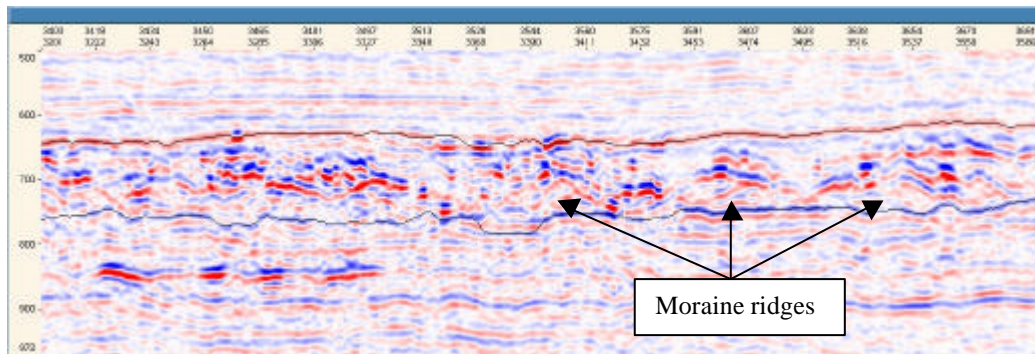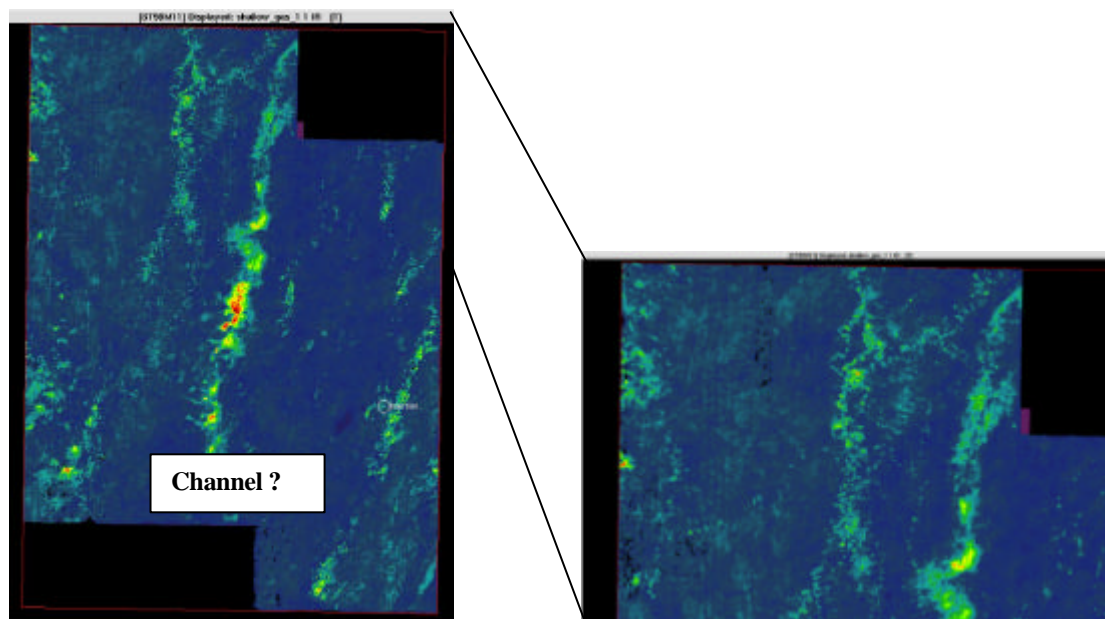rea. A zoomed image (right) of the northern central area shows that the channel structures have a clear meandering shape. The attribute was calculated in a constant time window.

Geometrical characterisation of the Upper Pliocene sediments with use of 3D Extrema classification

For characterisation of the central-north-eastern thickened area, 3D extrema classification was used to obtain a better image of the amplitude distribution and the structures that are believed to represent moraines. Figure 33(a) shows an inline section through this area where the classification result is compared with the seismic (Figure 33b). The green and yellow class is clearly reflecting the strong amplitude anomalies while the red class seems to define the surrounding part. Two maps are illustrated in Figure 34 which represent vertical counting of the green and yellow class (Figure 34a), and all three classes (Figure 34b) in the classified volume. The map with the two strong amplitude anomaly classes gives an impression of patchy / partly continuous moraine structures. The map with all three classes gives an impression of a more continuous moraine structures, especially the two structures indicated by arrows in Figure 34(b).

(a)

(b)
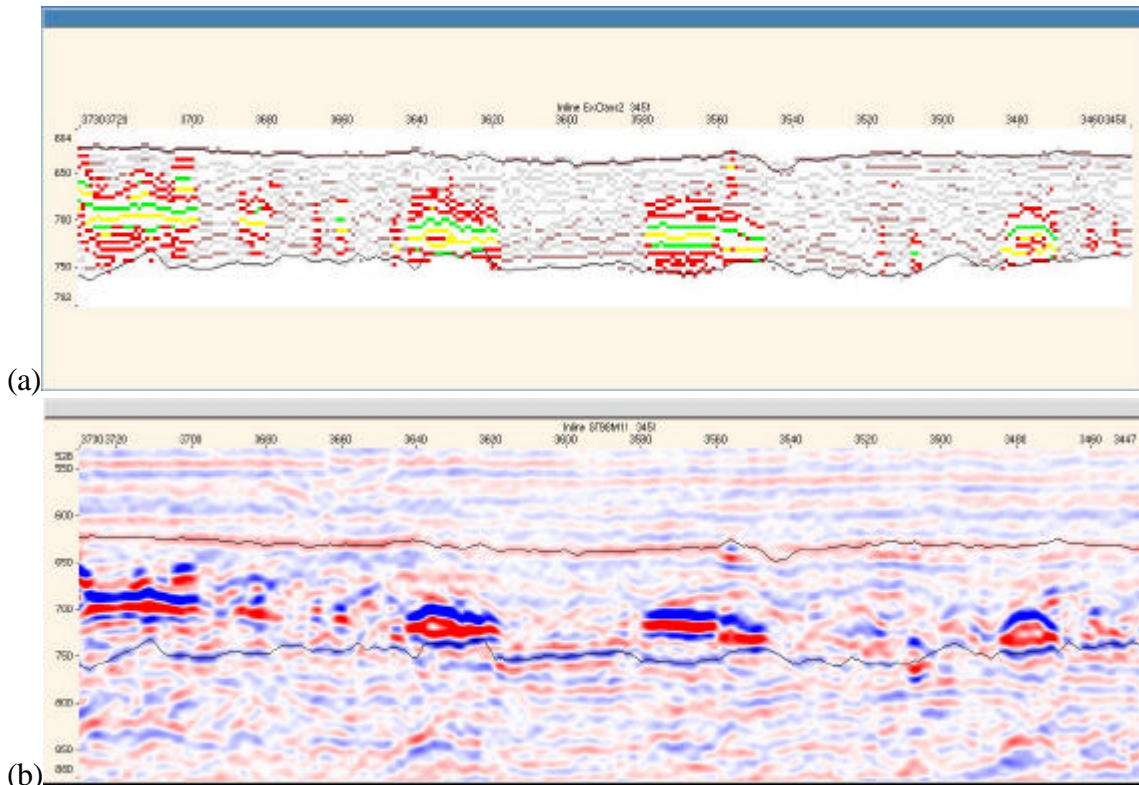
Figure 33 Inline section through the thickened moraine area showing the extrema classification (a), compared with the seismic (b). The green and yellow class reflects the strong amplitude anomalies while the red class defines the surrounding part. Together, these three classes seem to describe the main part of the moraine ridges. The location for this inline section is indicated with a white line on Figure 34.

Moraine ridges?
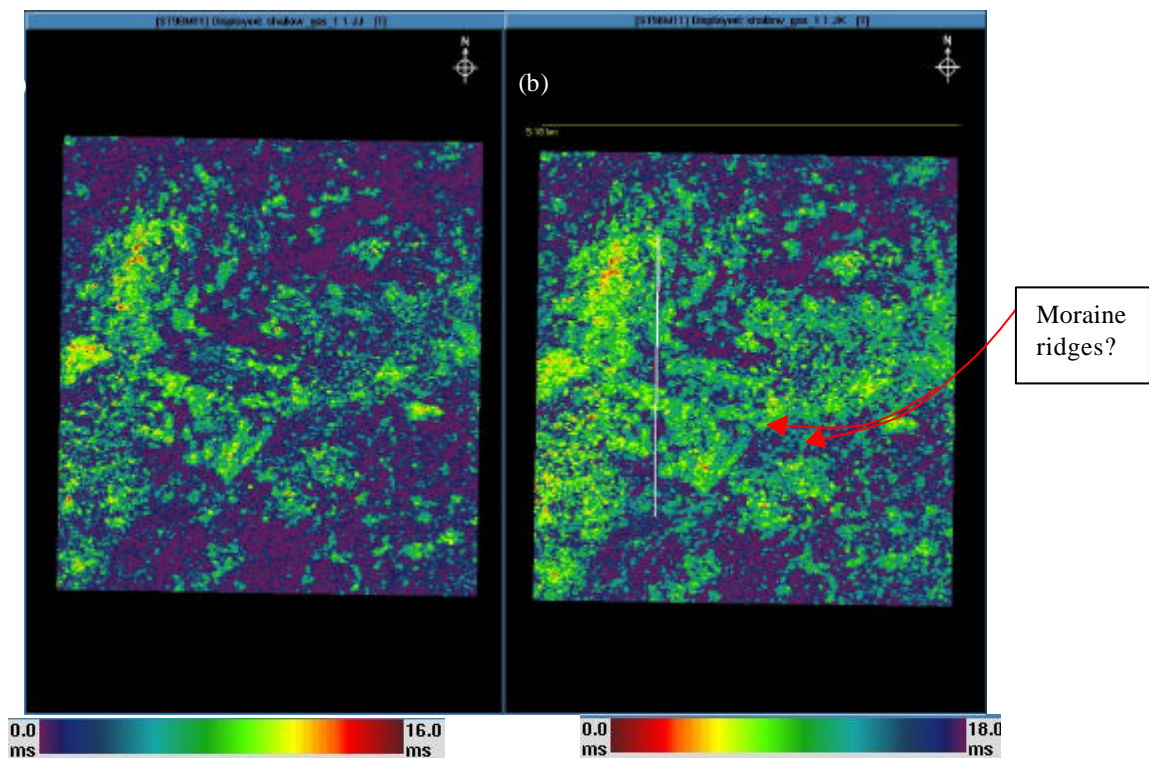
Figure 34 Maps that show a total count of the green and yellow class (a), and a total count of the green, yellow and red class (b), from Figure 33. The classes are counted vertically in the classified volume with a range between 0-16 (a) and 0-18 (b). The white line is indicating the position of the cross-section in figure 10.

A conclusion from these results is that the distribution of strong amplitude anomalies, and thereby the gas, are quite closely following the moraine structures, which again means that the moraine sediments are permeable to gas migration. When adding the third (red) class, a more continuous picture of the structures appears, meaning that this class represents moraine materials and/or shape.

Grid based classification of the gas distribution in the overburden

Grid based classification of different parts of the overburden was performed in order to map the distribution of gas, using the IMLE method. From a PCA analysis, the spectral component attributes: VRS 1, 2, 3. 4, 5 and 8 where chosen as a "standard attribute set" for all the classification runs. Different number of classes where tested out. 4 classes gave the best result in most cases and were preferred for all the final classification results. One of the classes represents the gas while the other three are assumed to represent different lithologies or combination of different lithologies. The attributes were generated in a constant time window, since a varying size of the window would affect the classification result.

Based on observations of the strong amplitude anomalies in the overburden, three grid-defined volumes with constant window size were defined. Since these volumes are not consistent with seismic stratigraphic boundaries, they are named Volume 1, 2 and 3.
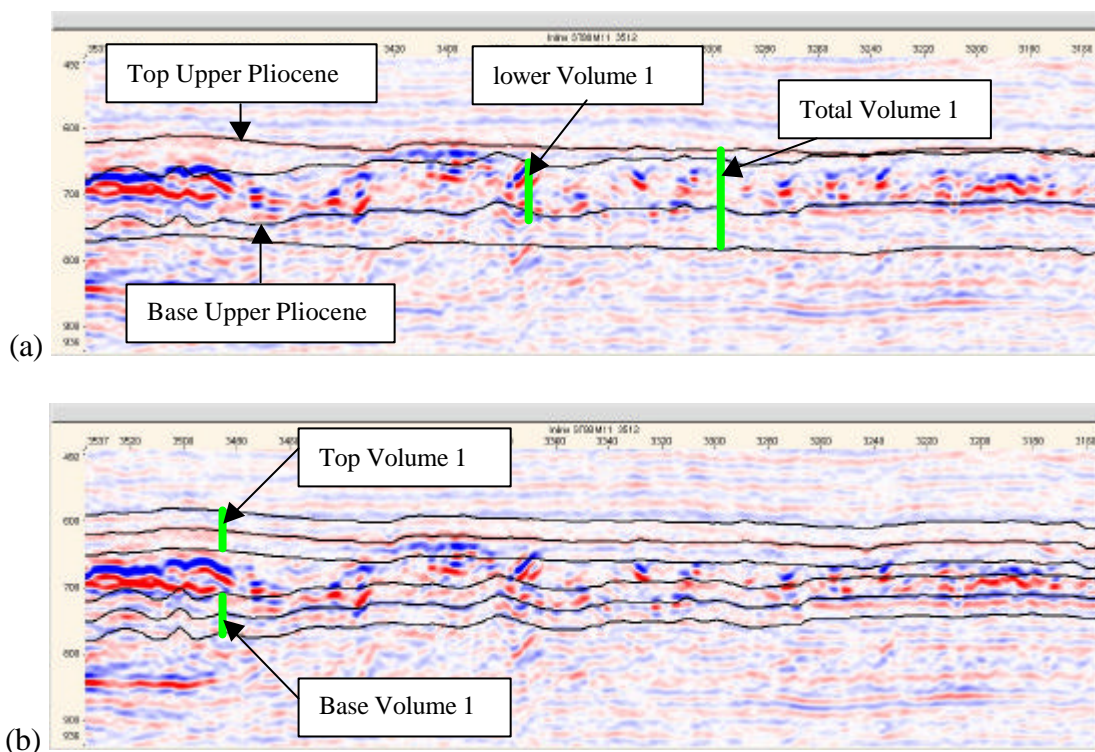
Figure 35 Volume 1 (V1) captures the Upper Pliocene Sediments. V1 is further subdivided into Total V1 and Lower V1 in figure (a), Top V1 and Bottom V1 in figure (b).

- Volume 1 (V1) covers the entire Upper Pliocene package. This volume is further divided into four sub-volumes with constant window size covering the "Total", the "Lower", the "Bottom" and the "Top" part, of the Upper Pliocene sediments (Figure 35). For the Total V1 (150ms), the geometry of the volume window was defined by the Top Upper Pliocene horizon. In most of the area, this volume captures also the upper part of the Lower Pliocene sediments. For the Lower V1 (75ms), the

geometry was defined by the Base Upper Pliocene horizon, and cover most of the Upper Pliocene sediments except in the thickened area. The Top V1 and the Base V1 was respectively defined by the top and base horizons of the Upper Pliocene, with a window size of 60ms each.

- Volume 2 defines a 35ms window in the Lower Pliocene sediments, following the geometry of the Top Utsira horizon (Figure 36).
- Volume 3 defines a 30ms window that captures The Top Utsira reflection (Figure 36).

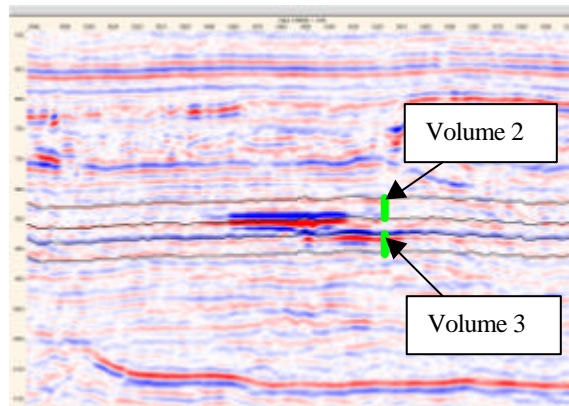Figure 36 Volume 2 is defined by a 35ms window and follows the geometry of the Top Utsira horizon. Volume 3 is defined by a 30ms window, which capture the top of the Utsira Sand.

Results from the classification of Volume 1
- The classification results from the Total V1 (Figure 37a) shows that the main part of the red gas class is reflecting both the NNE-SSW oriented channel structures and the moraine area (the thickened part), as observed from the amplitude maps (Figure 30 and Figure 32). Considerable parts of the gas class can also be observed in the north-east and south-west corner of the survey area. In the south-east part of the area, the gas distribution tends to be affected by the plough mark lineaments.
- The channel structure is not visible from the Lower V1 (Figure 37b), which indicates that this gas accumulation is only lying in the uppermost part of the Upper Pliocene sediments. In the thickened area, the gas distribution seems to be partly affected by the moraine structures. In the north-east and south-west corner, the gas class is more concentrated compared to the Total V1 distribution. The south-east part is affected by the plough mark lineaments.
- The plough mark lineament pattern is strongly indicated by the different classes in the Bottom V1 (Figure 37c) but the gas class distribution seems only to be partly affected by the lineaments. Concentrated gas distribution is still obvious in the north-east and south-west corner. Concentration of the gas class is also obvious in the moraine area.
- From the Top V1 (Figure 37d), the channel structures are reflected by the gas class as expected. Concentrated gas distribution is also obvious in the south-west and south-east corner. Gas is nearly absent in the moraine area.
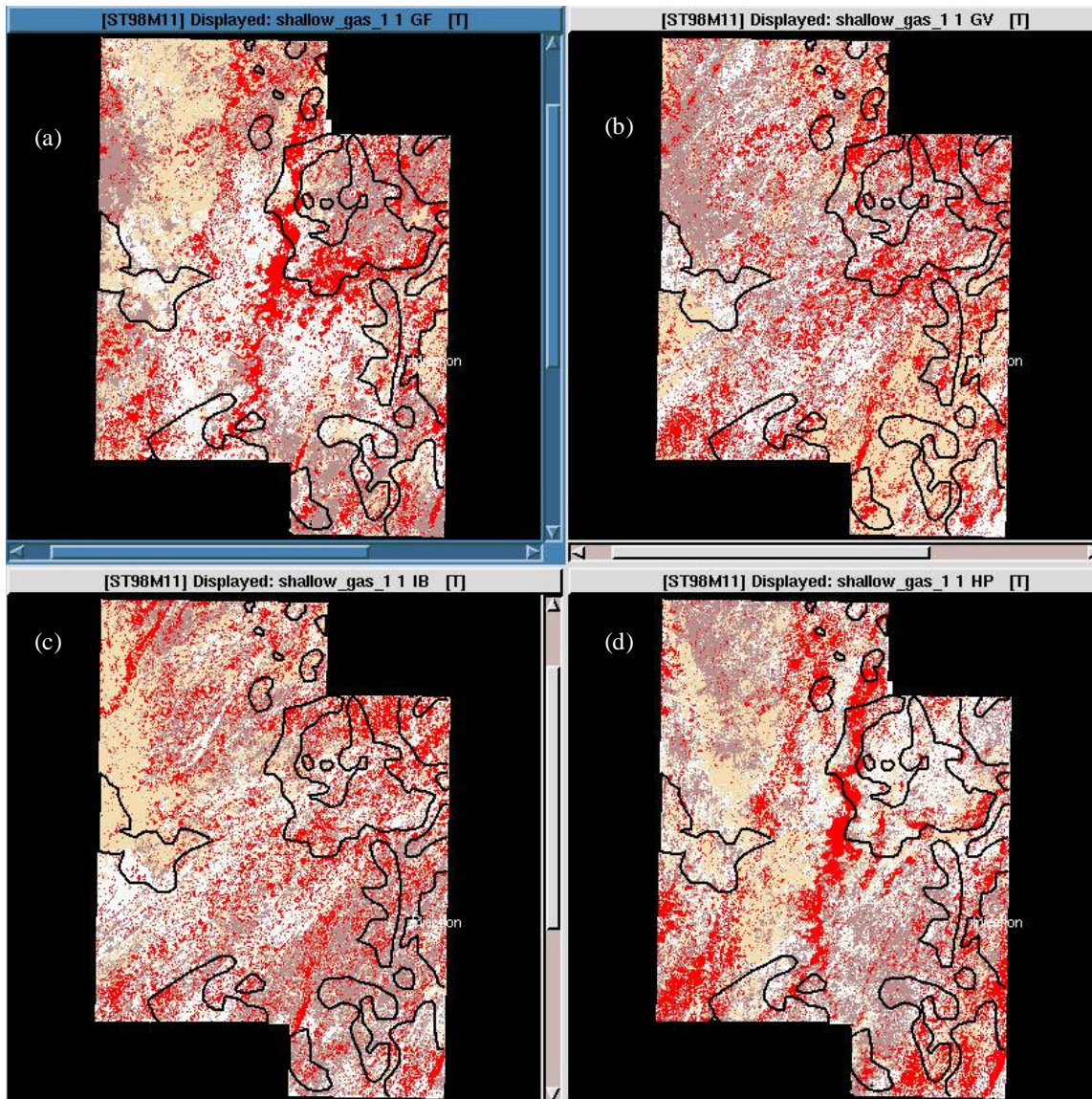
Figure 37 Classification results of Total V1(a), Lower V1(b), Bottom V1(c) and Top V1(d). The gas class is indicated by the red colour while the other three colours represent unidentified classes. The outline of the underlying mud volcanoes is indicated by black lines.

Summary of results from Volume 1 and correlation to mud volcano positions

In general, the dominating gas filled parts in Volume 1 are positioned in the moraine area, the north-east corner, the south-west corner and partly in the south-east part of the ST98M11 survey area. Major gas accumulations are also trapped in the channel structures in the uppermost part.

To relate the gas distributions in Volume 1 to the underlying positions of the main mud volcanoes, the outline of these volcanoes are plotted upon the classification maps in Figure 37. Most of the mud volcanoes are positioned in the east part. Two volcanoes are positioned in the south-west part, while no volcanoes are positioned in the north-west part.

In the north-east part, two major volcanoes (including the largest one) are correlating quite good with the moraine area, the north-east corner and parts of the largest channel structure. In general, the major gas accumulations are partly overlapping the mud volcano positions in this area. The gas accumulations are also partly overlapping the volcano positions in the south-east part, at least when considering the Top V1

(Figure 37d). In the south-west part, the gas seems to be positioned between the two volcanoes and shows nearly no overlap. The reason for this may be that the gas is trapped in the locally shallowest areas. Figure 38 shows that the geometry of Top Upper Pliocene horizon is closely affected by the underlying mud volcanoes, similar as shown for the Top Utsira horizon. If the flow connectivity is locally good in the Upper Pliocene sediments, a gas migration towards the locally highs is likely. The north-west area represents the least gas filled part of Volume 1. This gives confidence to leakage hypothesis since no underlying volcanoes are positioned in the same area.
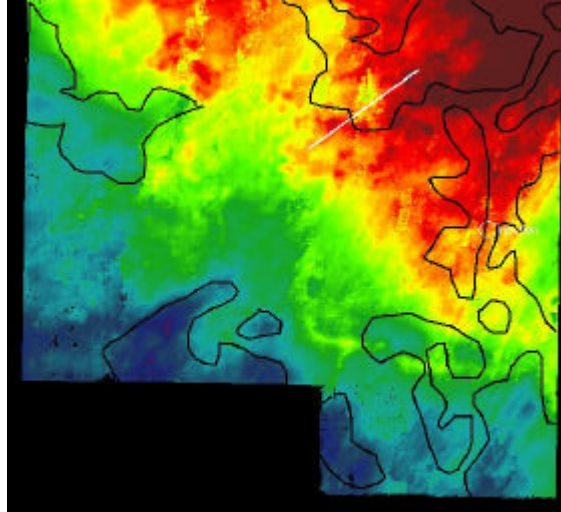

Figure 38 Horizon time map of Top Upper Pliocene in the SW corner of the ST98M11 survey area, shows that the horizon geometry is closely affected by the underlying mud volcanoes. Outline of the mud volcanoes is indicated by black lines. The colour scale is compressed.

Results from classification of Volume 2 and 3
- The gas class in Volume 2 is shown as distinct spots on the classification map (Figure 39a), fairly uniformly distributed over the survey area. The central-western part is weakly dominating the gas distribution. An interesting structure is represented by the brown class, which reflects a N-S trending wide structure in the eastern area. So far, this structure has not been related to any geometrical or lithological effect of the layers captured inside the volume.
- The gas distribution in Volume 3 (Figure 39b) is less concentrated compared to Volume 2, and is dominating in the west and north-west area. In the north-west area, the gas reflects a very distinct NNE-SSW elongated structure with sharply defined boundaries. The structure is probably representing a kind of stratigraphic trap.
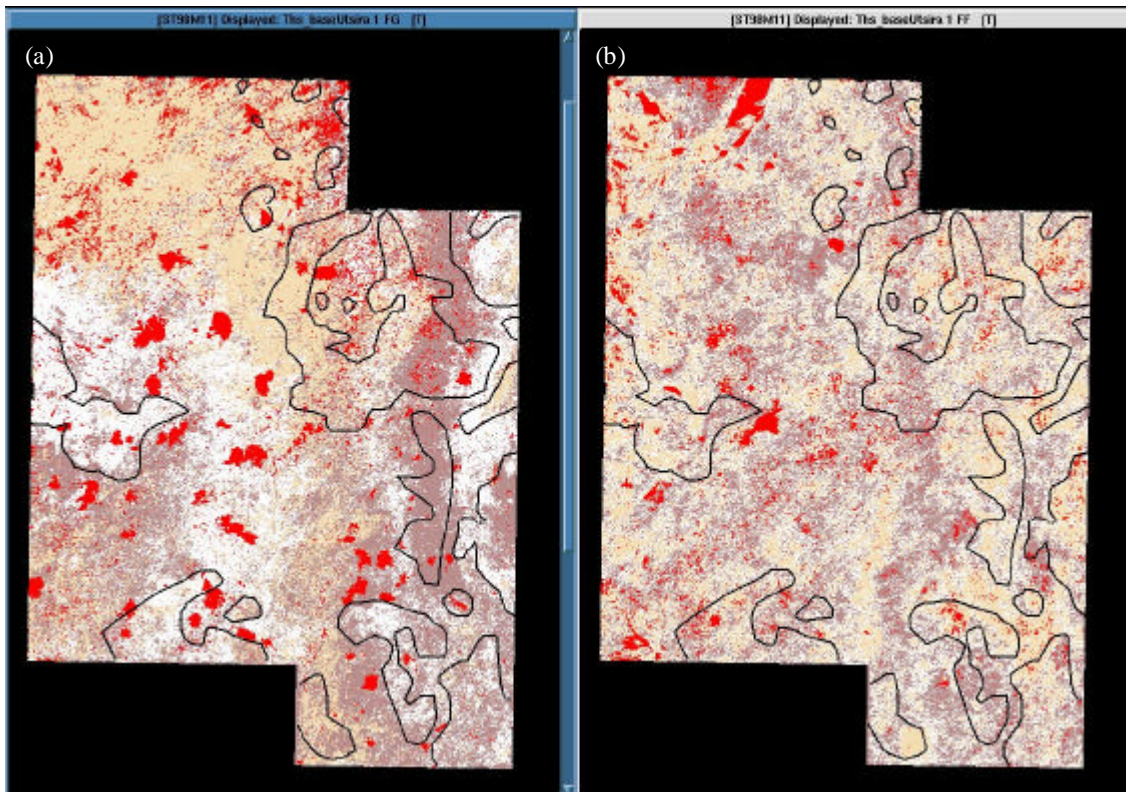
Figure 39 Classification results of Volume 2(a) and Volume 3(b). Red colour indicates gas. Black lines indicated the outlines of the mud volcanoes.
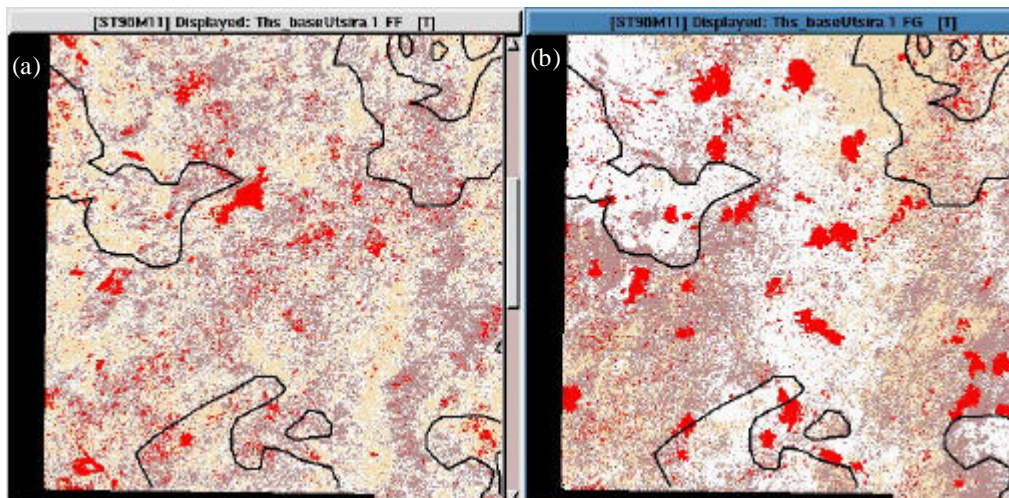
Figure 40 Detailed view of the classification results of Volume 2(a) and Volume 3(b) from the SW corner of the ST98M11 survey area.

Summary of results from Volume 2 and 3, and correlation to mud volcano positions
Volume 2 and Volume 3 shows some degree of correlation in gas positions in the south-west part of the survey area (Figure 40). In both volumes, the gas seems to be distributed outside of the two volcano positions in the same area. This coincides with the trend observed from Volume 1, which gives confidence to the gas leakage hypothesis. In the north-west corner, a small area of gas is observed from Volume 2 while a larger area is obvious from Volume 3. This observation from Volume 3 is also different from the general trend observed from Volume 1. Since the Utsira Sand has a general high permeability and connectivity in the survey area, the explanation for the gas accumulation may be that it's a structural high area, and therefore the gas may have migrated from other structurally lower areas.

Concluding points

- The CO_2, partly sealed by thin shale layers in the Utsira Sand, have been successfully mapped in great detail in the 1999 and the 2001 seismic data. An expansion of the CO_2 between 1999 and 2001 is obvious.

- From use of the SED attribute technique, creating energy-difference maps of each CO_2 accumulation, it is possible to study CO_2 flow pattern. The flow of CO_2 is clearly affected by linear flow boundaries, most possibly representing both faults and stratigraphic structures like channels.

- From use of 3D extrema classification, mapping of a poorly defined reflection in the Utsira Sand was performed. Horizon interpretation on the extrema class made it easier to map this particular horizon in 3D. Gaps in the class consistent horizon extraction revealed possible sub-seismic structures, which are important regarding the CO_2 flow pattern.

- The overburden analysis revealed that much of the gas accumulation is trapped in structures that most possibly represent a glacial moraine complex and a channel complex. The distribution of gas in the moraine complex was successfully mapped in detail with use of the 3D extrema classification technique.

- With use of the grid-based classification method, distribution of gas was mapped in the different parts of overburden. The gas positions where correlated with the underlying mud volcano positions. In a regional sense, the gas positions showed some degree of vertical correlation with each other and with the mud volcanoes, but the correlation result is not convincing. If the leakage hypothesis should be verified only on the basis of gas accumulation correlation, a much more closer correlation match should be expected.

Shale seal quality estimation by Super Resolution mapping

Super Resolution mapping has been applied to study the thickness of the sealing shale layer above the Utsira formation, to investigate possible leakage zones in the shale. The baseline data (Mig_94 and Mig_94_01, respectively the 1999 and 2001 re-processed versions of the baseline-survey) are used. The thickness of the shale layer and the sand wedge above is small, resulting in tuning effects in the seismic signal. The Super Resolution algorithm is constructed to deal with tuning problems, and aims at deconvolving the interference in the seismic signal. The deconvolution is performed assuming the number of reflectors and the wavelet is known. The wavelet is extracted using our patent pending 3D blind deconvolution (3DBD).

The top of the Utsira formation is interpreted on a negative event on the seismic cube, and the top of the sand wedge as the next negative event above top Utsira. The positive event in between is assumed to be the result of interference between these two reflectors and the base of the sand wedge. Super Resolution mapping is used to determine the exact position of the base of the sand wedge in the tuning region, with the top of the sand wedge and the top of Utsira interpreted in advance.

The Super Resolution algorithm was first run on the 1999-re-processed version of the baseline seismic, Mig_94. Figure 41 shows an inline section through the seismic cube, with the pre-interpreted reflectors and the interpretation obtained using Super Resolution. The result shows some variations in the shale layer thickness, with smaller regions where the shale layer is very thin. The algorithm was next run on the 2001-re-processed baseline data, Mig_94_01, in a region above the injection point: inlines 3751-3950, crosslines 3051-3300. Figure 42 shows the interpretation in an inline section, Figure 43a shows the resulting thickness of the shale layer and Figure 43b the thickness of the sand wedge. For Mig_94_01 the interpreted base of the sand wedge is smoother than on the original data, and the shale layer thickness varies less. The shale layer thickness in Figure 43a shows some variations in thickness laterally, but for the Mig_94_01 seismic cube the interpretations do not reveal any obvious leakage points in the shale layer in the region where the leakage is observed on the time lapse data. The different results for the two different

baseline seismic cubes may be a result of the noise level in the seismic data, or may be related to differences in the estimated wavelets for the two cubes.

Figure 41 Seismic inline section (Mig_94) showing the Super Resolution mapping of the base of the sand wedge. The top and bottom reflectors are interpreted in advance, and are used as input to the algorithm.
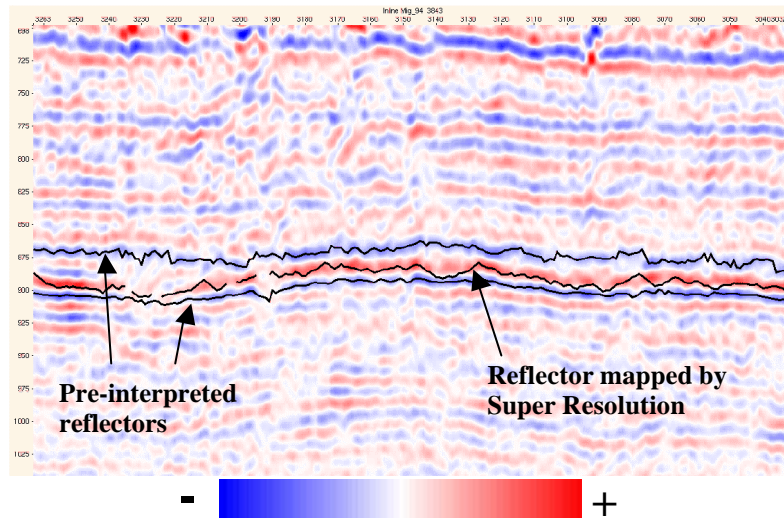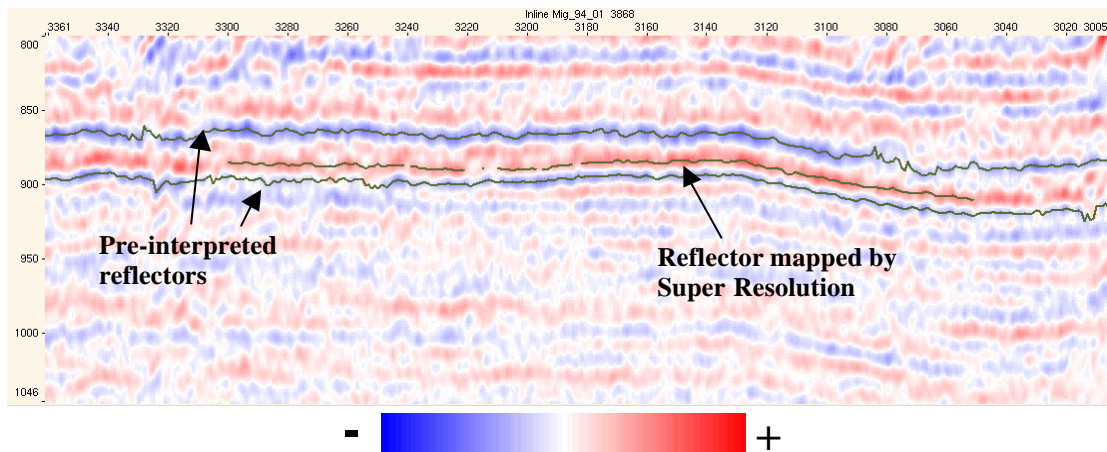

Figure 42 Seismic inline section (Mig_94_01) showing the Super Resolution mapping of the base of the sand wedge. The top and bottom reflectors are interpreted in advance, and are used as input to the algorithm.
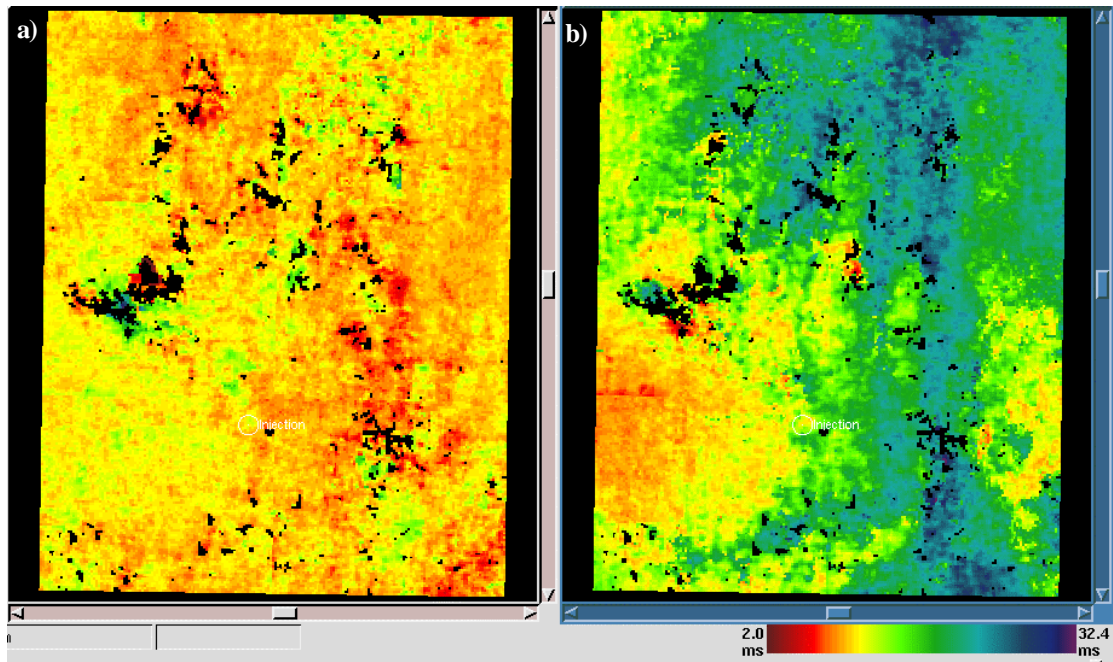
Figure 43 Thickness of a) shale layer and b) sand wedge on Mig_94_01.

Top and base CO₂ pocket detection by Super Resolution mapping

For thin layers of CO_2, the reflection from the top and base of the CO_2 pocket will result in interference in the seismic signal. Super Resolution mapping is applied, trying to map the vertical extent of some of the CO_2 pockets on the 1999 and 2001 time-lapse data (Mig_99_01, Mig_01). Results from 3D blind deconvolution are used as input to the Super Resolution algorithm.

3D blind deconvolution

3D blind deconvolution (3DBD) is run prior to Super Resolution, on both time lapse surveys (Mig_99_01, Mig_01), in a volume covering the injected CO_2. 3DBD is applied to extract the wavelets required as input to Super Resolution, and the two wavelets for the 1999 and 2001 surveys are shown in Figure 44. Furthermore, the reflectivity estimates from 3DBD, shown in Figure 45, reveal which seismic maxima and minima are actual reflectors and which are more likely to be side lobes. These results indicate the positions of the CO_2 pockets, and help determine in which regions Super Resolution should be applied to continuously map the top and base of the CO_2 pockets.
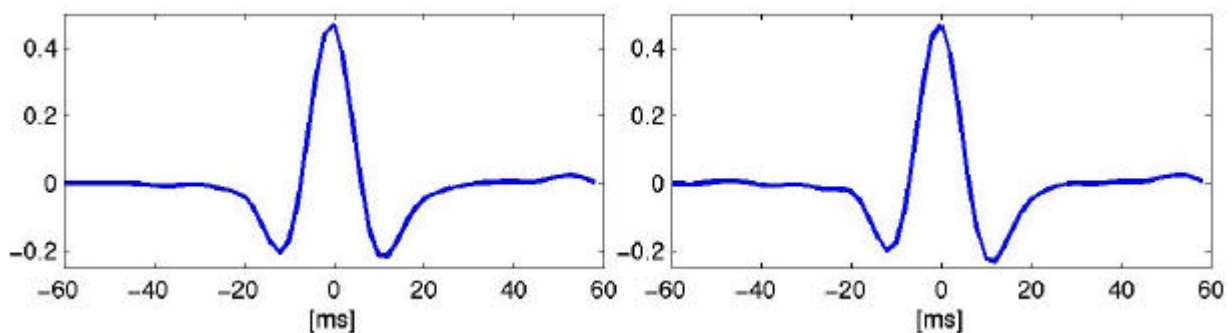

Figure 44 Wavelets extracted from the seismic cubes Mig_99_01 (left) and Mig_01 (right).
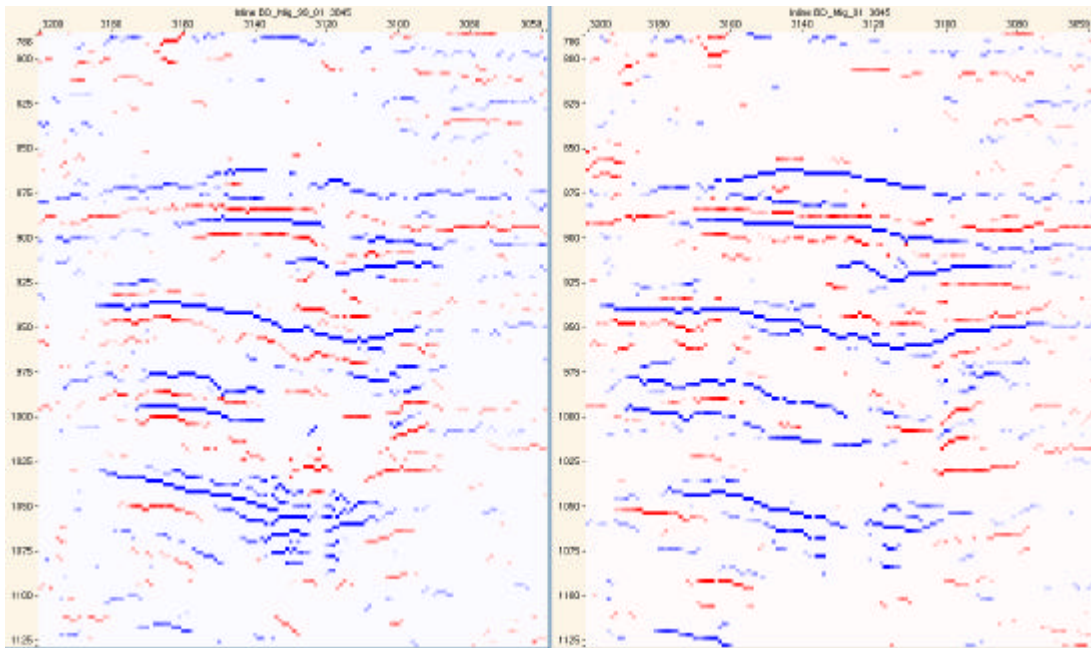
Figure 45 Inline sections through the reflectivity cubes generated by 3D blind deconvolution from the seismic cubes Mig_99_01 (left) and Mig_01 (right).

Top and base CO$_2$ Super Resolution mapping

Reflectors from CO$_2$ pockets should appear as pairs of reflectors, negative above positive. Some potential reflectors from CO$_2$ pockets are interpreted from the reflectivity cubes in Figure 45, and Super Resolution mapping is run in these regions. The algorithm is run once for each CO$_2$ pocket. The results are shown in Figure 46, illustrated on an inline section from the seismic cubes Mig_99_01 and Mig_01. The thickness maps of the CO$_2$ pockets in Mig_99_01 are illustrated in Figure 47. Some of the mapped CO$_2$ pockets show clear tendencies of being thinned towards the rim of the pockets, as we would expect from a dome-geometrically confined CO$_2$ pocket. Not all CO$_2$ pockets are analysed using Super Resolution, and the main limitation is the complexity of the interference pattern arising when too many CO$_2$ pockets are closely spaced.

The Super Resolution algorithm is instructed to map two reflectors throughout a defined region of interest. In some regions of the CO$_2$ pockets shown in Figure 47, the resulting reflectors lies at a constant short distance of 2-4ms, related to a minimum allowed distance used in the algorithm. In these regions the results from Super Resolution are somewhat unreliable, indicating that the algorithm is not able to detect two well-defined, sufficiently separated reflectors. Note that the physical explanation can be either that the reflectors are very close or that there is no base CO$_2$ reflector in the examined interval.

Another test of the existence of a base CO$_2$ reflector corresponding to a large difference in CO$_2$ saturation is obtained by examining the amplitude of the identified potential base CO$_2$ reflectivity (keeping in mind the non-linear nature of the impedance with respect to CO$_2$ saturation). CO$_2$ pocket number 2 is examined. Figure 48 shows top and base CO$_2$ reflectivity maps obtained from the Super Resolution mapping, and a corresponding base reflectivity map obtained from the 3DBD cube. A reliable estimate of a large saturation difference will yield a large reflectivity. Low estimated reflectivity thus corresponds to either a small saturation difference or a low reliability estimate. It is observed from Figure 48 that the top CO$_2$ reflectivity is strongest in the middle and decreasing towards the rim. For the base CO$_2$ interpretation however, the central part has a low reflectivity, indicating lack of a high confidence base CO$_2$ reflector in this region. Similar effects are observed for some of the other CO$_2$ pockets, and in particular for pocket number 2 of the 2001 seismic cube (see Figure 45).
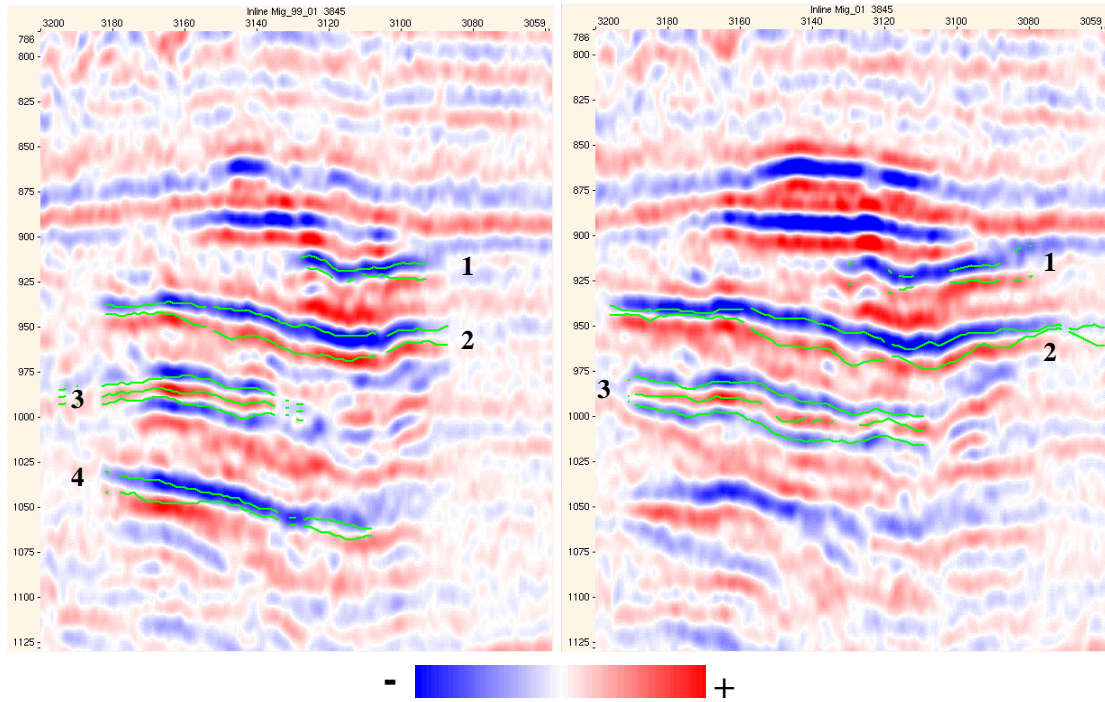
Figure 46 Inline sections from Mig_99_01 (left) and Mig_01 (right), showing the results from Super Resolution mapping of some of the CO_2 pockets.
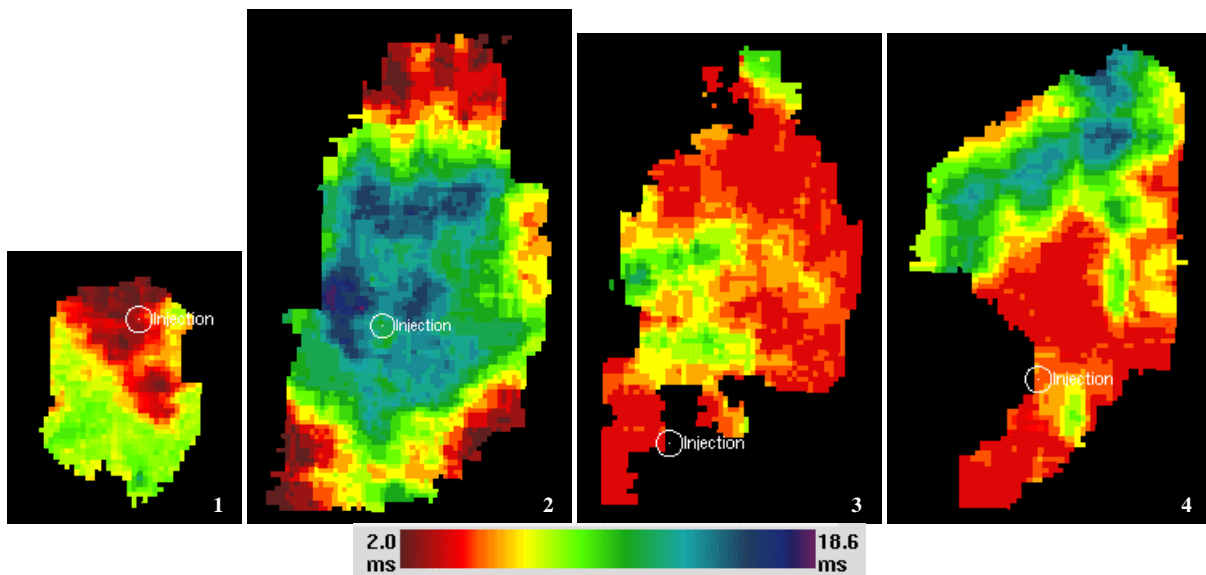

Figure 47 Thickness of CO_2 pockets from Mig_99_01 found by Super Resolution mapping. The numbering of the CO_2 pockets corresponds to the numbering in Figure 46.
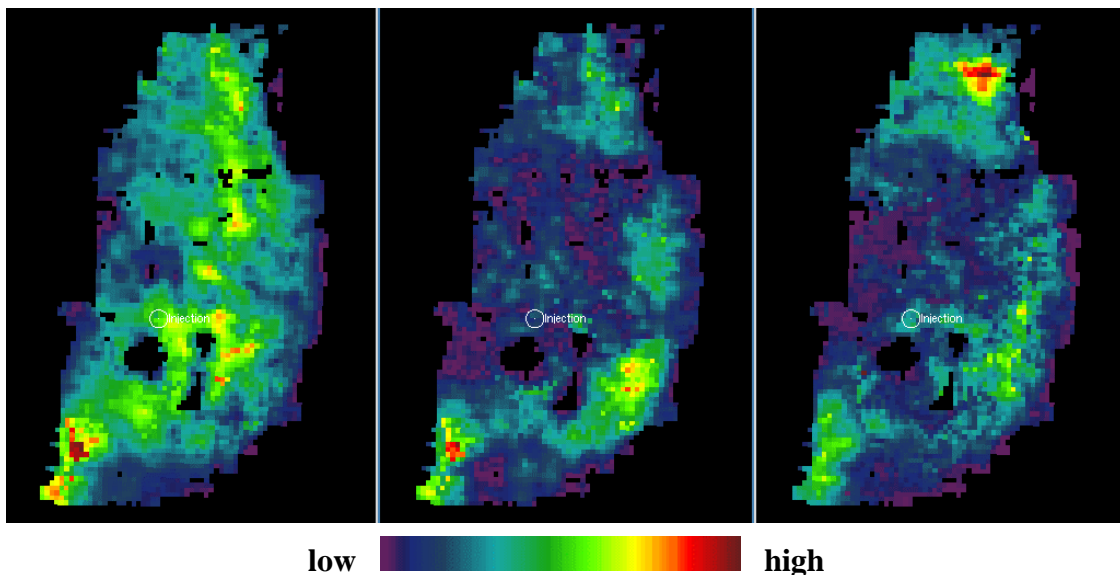
low high

Figure 48 Reflectivity at the top (left) and base (middle) CO_2 reflection events estimated from Super Resolution, and the corresponding base CO_2 reflection magnitude calculated within a pre-specified vertical displacement range from the 3DBD cube (right). The hypothesis is that in the middle and right figure, large amplitude reflects a high confidence base CO_2 reflector (corresponding to an interface of high to low CO_2 saturation), whereas low amplitude reflects that the zone below the CO_2 pocket has too high CO_2 saturation to create a significant seismic reflector.

Volume estimates from Super Resolution mapping

The number of voxels of the seismic cubes contained within each CO_2 pocket, i.e., between the top and base of a pocket, can be calculated based on the thickness maps in Figure 47. Regions with a minimal, constant distance between the two mapped reflectors are not included in the calculations, as the top and base estimates are unreliable in these regions (see discussion above). The actual volume of accumulated CO_2 within a pocket is estimated by multiplying the number of voxels of the pocket with the volume of CO_2 within each voxel:

$$\text{Vol}_{CO2} = dx \cdot dy \cdot \frac{dTWT \cdot V_g}{2} \cdot \boldsymbol{j} \cdot S_g$$

In this equation, dx and dy are the inline and crossline sampling distances, $dTWT$ is the height of the voxel measured in two-way travel time, V_g is the velocity in CO_2 saturated sandstone within the Utsira formation, $\boldsymbol{j}$ is the porosity and S_g is the CO_2 saturation. With $dx=dy=12.5$m, $dTWT=0.002$s, and assuming $V_g = 1400$m/s, $\boldsymbol{j} = 0.37$ and $S_g = 0.9$, the voxel volume of CO_2 is $\text{Vol}_{CO2}=72.84$m^3. For the 1999 seismic survey (Mig_99_01) the estimated CO_2 volumes of the pockets numbered 1-4 in Figure 46 and Figure 47 are 2.22×10^5 m^3, 14.3×10^5 m^3, 3.38×10^5 m^3 and 6.27×10^5 m^3 respectively. Only the volume of pockets 1 and 2 are estimated for the 2001 survey (Mig_01), resulting in the volumes 6.09×10^5 m^3 and 19.1×10^5 m^3.

Conclusions

The top and base of a number of CO_2 pockets have been mapped using the Super Resolution algorithm, on both the 1999 and 2001 seismic surveys. The main observations from this work are: We are able to map CO_2 pockets that are thickest in the central parts, and thinning out towards the rims. The CO_2 pockets typically have a strong reflectivity at the top, but the estimated base reflectivity tend to be weak, indicating lack of a high confidence base CO_2 reflector. The Super Resolution results have been applied to estimate volumes of CO_2 accumulated within each of the mapped pockets.

Pull-down analysis

In the CO_2 filled areas the acoustic velocity decreases relative to the baseline seismic. The wave-front retardation is due to the acoustic properties of the injected CO_2 gas, and it is observed as a "pull-down" of the seismic time-lapse signals in and below the CO_2 cloud. The amount of pull-down is estimated by comparing travel time interpretations of certain reference horizons in the baseline seismic with travel time interpretations of the corresponding horizons in the time-lapse seismic. Unfortunately, the signals are more or less discontinuous in and around the CO_2 cloud, and advanced automated 3D travel time extraction procedures would be needed to generate detailed interpretations of several horizons in the area of interest. In this work the interpretations are made manually with support from resolution-enhanced and extrema cubes created in GeoFrame™. As a starting point, we therefore restricted our interpretations to the following horizons: Top, Mid and Base Utsira, as well as Hordaland.
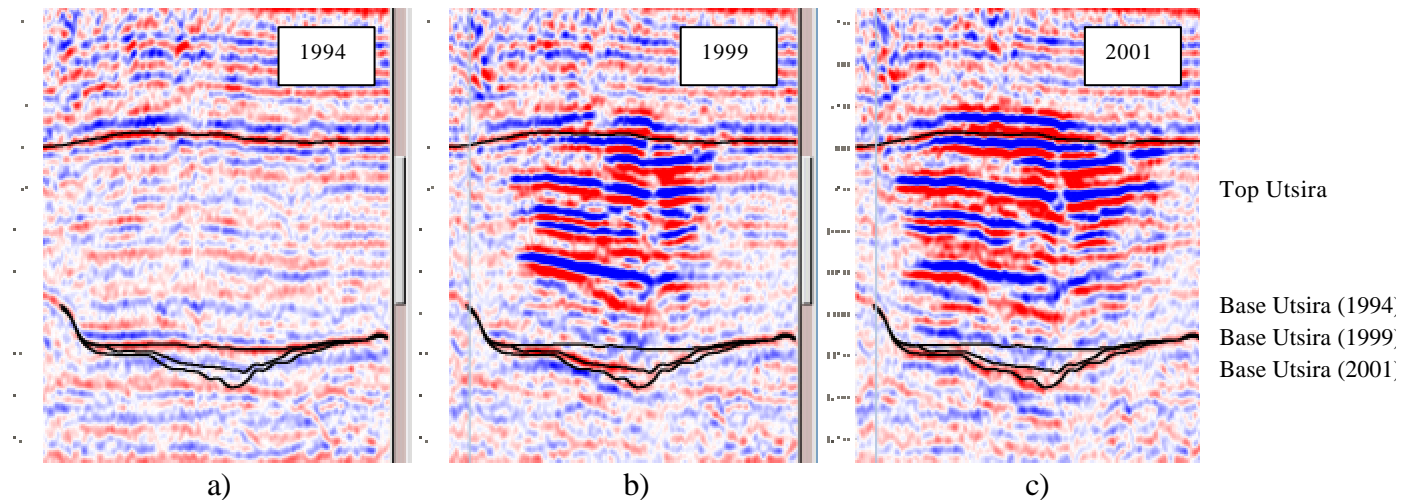

Figure 49 Travel time interpretations of Top Utsira (upper line) and Base Utsira (lower lines) plotted on top of a section of a) 1994 seismic, b) 1999 seismic and c) 2001 seismic crossing through the injection point. The upper line below the CO_2 cloud is the 1994 interpretation of Base Utsira. The middle line is the 1999 interpretation and the lower line is the 2001 interpretation of Base Utsira.

We have made consistent interpretations of Top and Base Utsira for the three data sets available: 1994, 1999 and 2001[1]. As the CO_2 is mainly located below Top Utsira the interpretation of this horizon is taken to be the same for all data sets. The upper black line in each of the three plots in Figure 49 shows the interpretation of Top Utsira. The baseline and time-lapse interpretations of Base Utsira are represented by the upper, middle and lower lines in the lower half of Figure 49. In Figure 50 a grid plot of the Top Utsira interpretation is displayed, and in Figure 51 grid plots of the baseline and time-lapse interpretations of Base Utsira can be seen. The amount of pull-down caused by the injected CO_2 can be observed from the travel time difference between each of the Base Utsira interpretations. In Figure 52 the travel time differences between the time-lapse interpretations and the baseline interpretation are shown as grids. Note the conformity in shape between Top Utsira in Figure 50 and the CO_2 distribution indicated by the pull-down in Figure 51 and Figure 52. Due to noise and discontinuity of the signal in the injection area and below Base Utsira, no reliable interpretations were obtained for Mid Utsira and Hordaland.

---

[1] To ensure that all the data is processed by the same procedure the 1994 and 1999 data sets were re-processed simultaneously with the 2001 data.
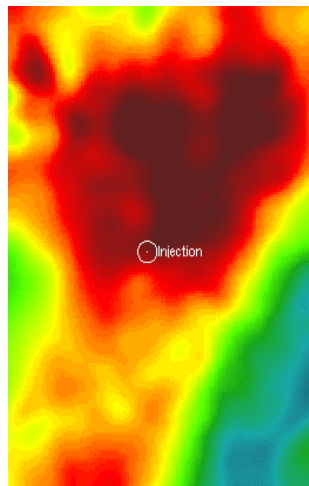
Figure 50 Interpretation of Top Utsira on the 1994 data. The colour scale indicates the travel time. The injection point is marked in the middle of the figure, and the grid covers the same area as the grids displayed in Figure 51 and Figure 52.
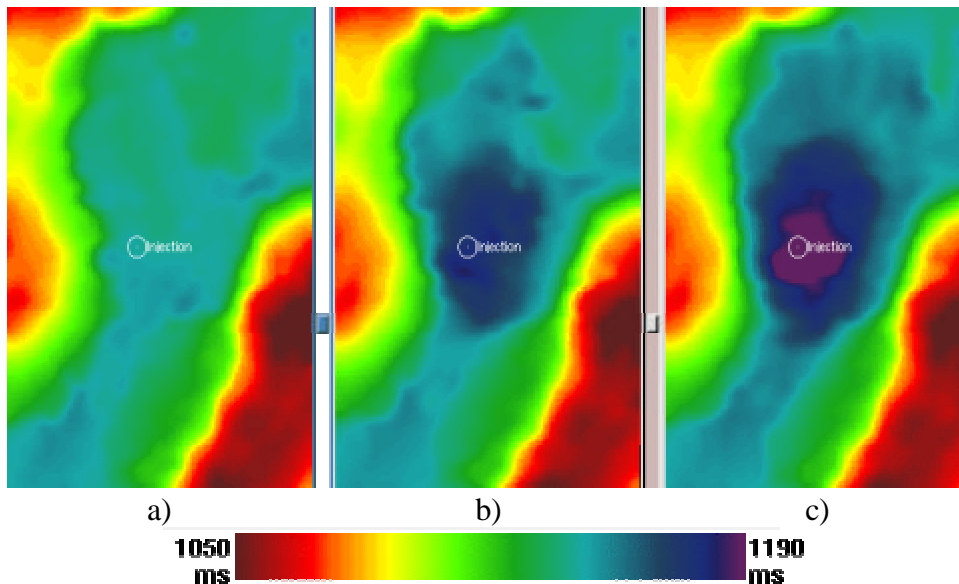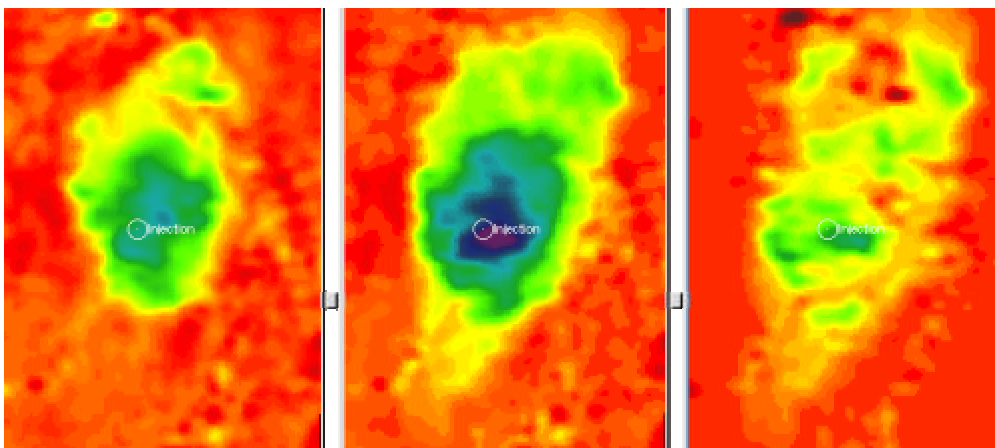

Figure 51 Interpretations of Base Utsira on the a) 1994 data, b) 1999 data and c) 2001 data. The colour scale indicates the travel time. The injection point is marked in the middle of each figure, and the grids cover the same area as the grids displayed in Figure 50 and Figure 52.
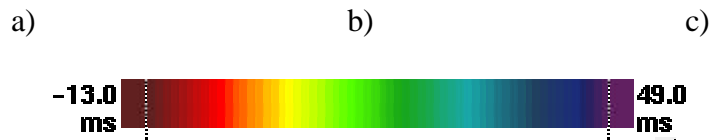
Figure 52 The interpretations of Base Utsira are subtracted from each other to obtain travel time difference plots: a) 1994 interpretation subtracted from 1999 interpretation, b) 1994 interpretation subtracted from 1999 interpretation and c) 1999 interpretation subtracted from 2001 interpretation. The injection point is marked in the middle of each figure, and the grids cover the same are as the grids displayed in Figure 50 and Figure 51.
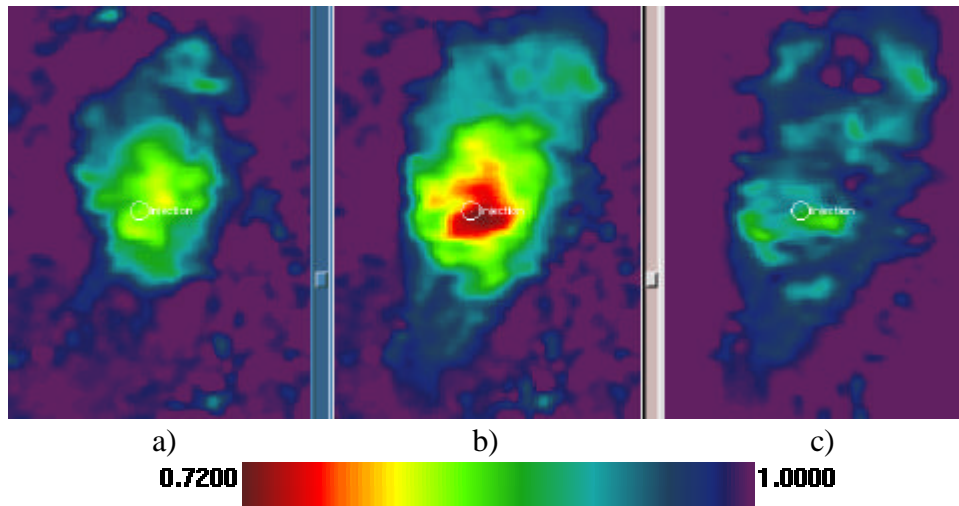

Figure 53 Relative P-velocity changes in the interval between Top and Base Utsira a) from 1994 to 1999, b) from 1994 to 2001 and c) from 1999 to 2001. The relative velocity changes are indicated by the colour scale above. The injection point is marked in the middle of each figure, and the grids cover the same area as the grids displayed in Figure 50, Figure 51, and Figure 52.

Estimation of relative interval velocity changes in the CO$_2$ zone

The relative interval velocity changes in the CO$_2$ zone have been estimated based on 3D post-stack travel-time interpretation of the three data sets available. The relative velocity changes are estimated by a procedure called Vertical Seismic Scaling (VSS)[2] that calculates the relative velocity changes from the time-lapse differences in travel-time within a layer bounded by two horizons. Detailed interpretations are required as input to the VSS procedure in order to obtain plausible estimates of the velocity changes. Moreover, a higher velocity resolution is obtained if a thick layer is subdivided into thinner layers.

As mentioned in the above paragraph, we have only been able to find detailed and consistent interpretations of Top and Base Utsira for all data sets. The relative P-velocity changes for the interval between Top and Base Utsira are shown in Figure 53. Note the resemblance between the grids in Figure 52 and the corresponding grids in Figure 53. Due to noise and discontinuity of the signal in the injection area and below Base Utsira, no interval velocity changes were estimated for the two subintervals within the Utsira layer or for the interval between Base Utsira and Hordaland.

---

[2] The VSS procedure is developed by Schlumberger Stavanger Research and is available in the GeoFrame 3.8 and 4.0 software packages.

As indicated by the name of the VSS procedure, it also creates "scaled seismic" that can be used to assess the probability that the interpretations are plausible. The time-lapse seismic is stretched vertically according to the travel time difference between the time-lapse interpretation and a chosen reference interpretation. (In this case the interpretation made on the 1994 data is used as a reference interpretation as this data set was acquired before the gas injection commenced). If the stretched version of the time-lapse seismic is approximately equal to the reference seismic this may indicate that the time-lapse interpretation is reliable. The interpretations of Base Utsira are evaluated by comparing the reference seismic to the time-lapse seismic obtained by using VSS.

Velocity model building using tomography.

We have used tomography and 3D pre-stack depth migration for velocity model building. Pre-stack depth migration handles lateral velocity variations much better than conventional time processing techniques. The objective criterion for estimating the correct velocity model is whether
all events on the common image point (CIP) gathers are flat, implying that we obtain consistent depth images for all vintages.

CO_2 clouds are particularly difficult to deal with – they often cause severe velocity anomalies but, as the clouds do not have distinct boundaries, it can be very hard to define the extent of the cloud and so model the anomaly. If the CO_2 cloud can be adequately represented in the velocity model, it is possible to compensate for it's effect and flatten the events on the CIP-gathers. See Figure 54 for an intermediate result.

Currently we obtain nice and flat events in the CO2 affected area, but events below the CO2, as well as on the rims of the CO2 cloud are not yet correctly positioned. The analysis is not completed yet, but our preliminary conclusion is that satisfactory velocity models for the 1999 and 2001 data are not yet obtained. The analysis will continue beyond the end of the project on our own account.
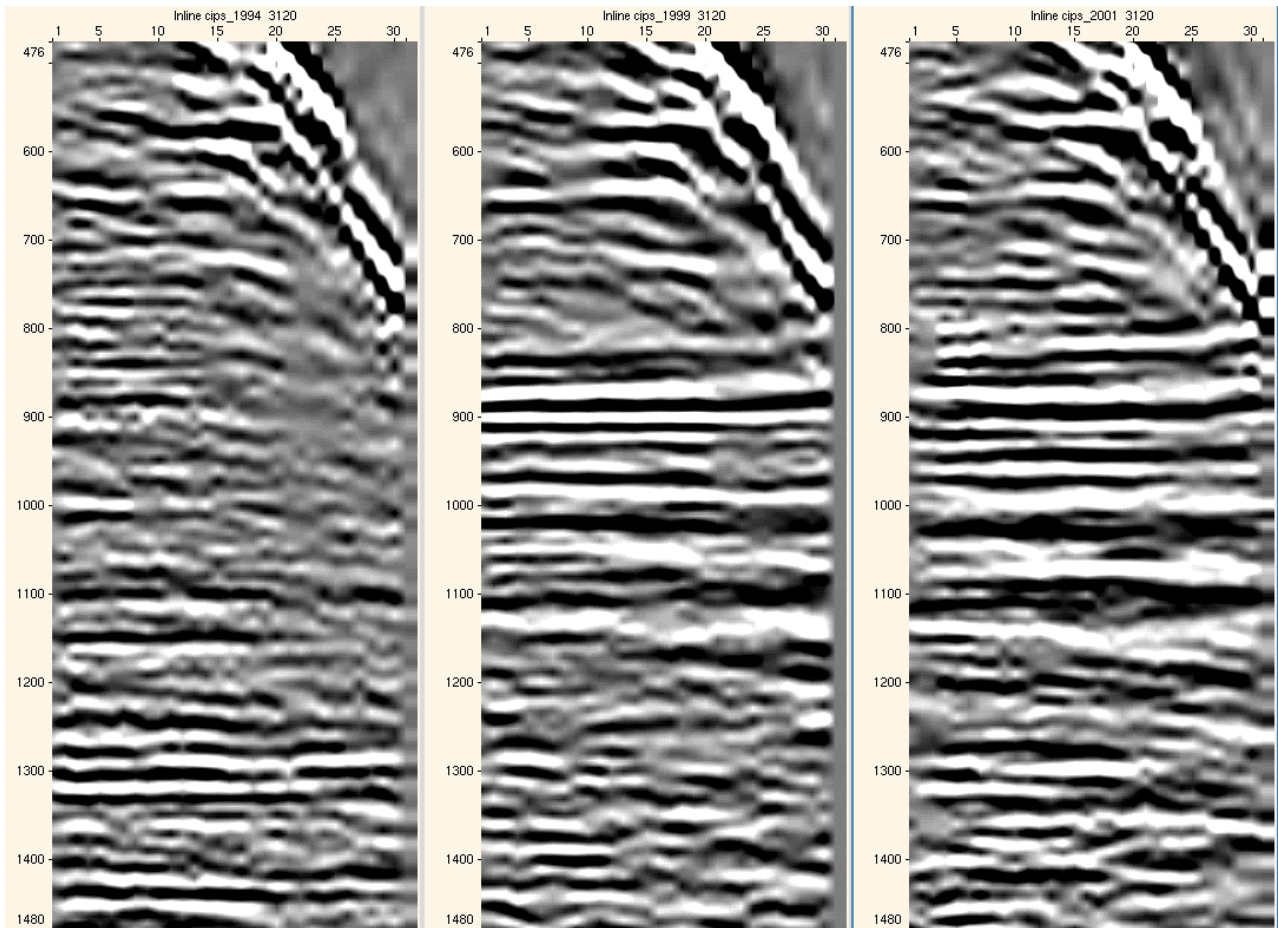
Figure 54 CIP gathers in the current status of the tomographic inversion and 3D pre-stack depth migration work.

Integration of time-lapse seismic with reservoir flow model

Time-lapse data may be compared to results from a simulator with the aim to improve the flow model. Subsequent predictions of reservoir behaviour will then be more accurate. Such a "4D seismic history match" is illustrated by the optimisation loop in Figure 55. In this loop time-lapse seismic data is evaluated against results from the flow model. From this evaluation an objective function is constructed as a measure for the difference between the 4D seismic and the flow model. An optimisation algorithm then tries to minimise the objective function by altering a given set of parameters in the model.

A reservoir flow model was developed by Lindeberg *et al*., (2000) in order to study the dominant flow processes. The predicted CO_2 distribution was matched with the seismic in an iterative process. The matching consisted in predicting the same number of CO_2 accumulations and approximately the same extension of the individual accumulations as observed from the time-lapse seismic.
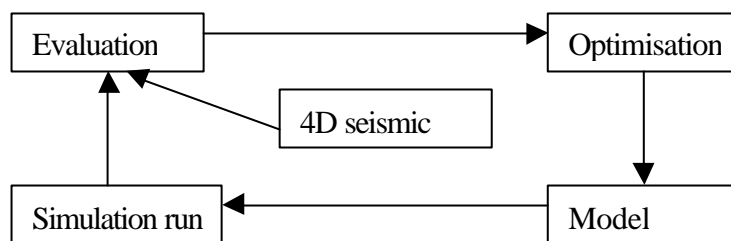

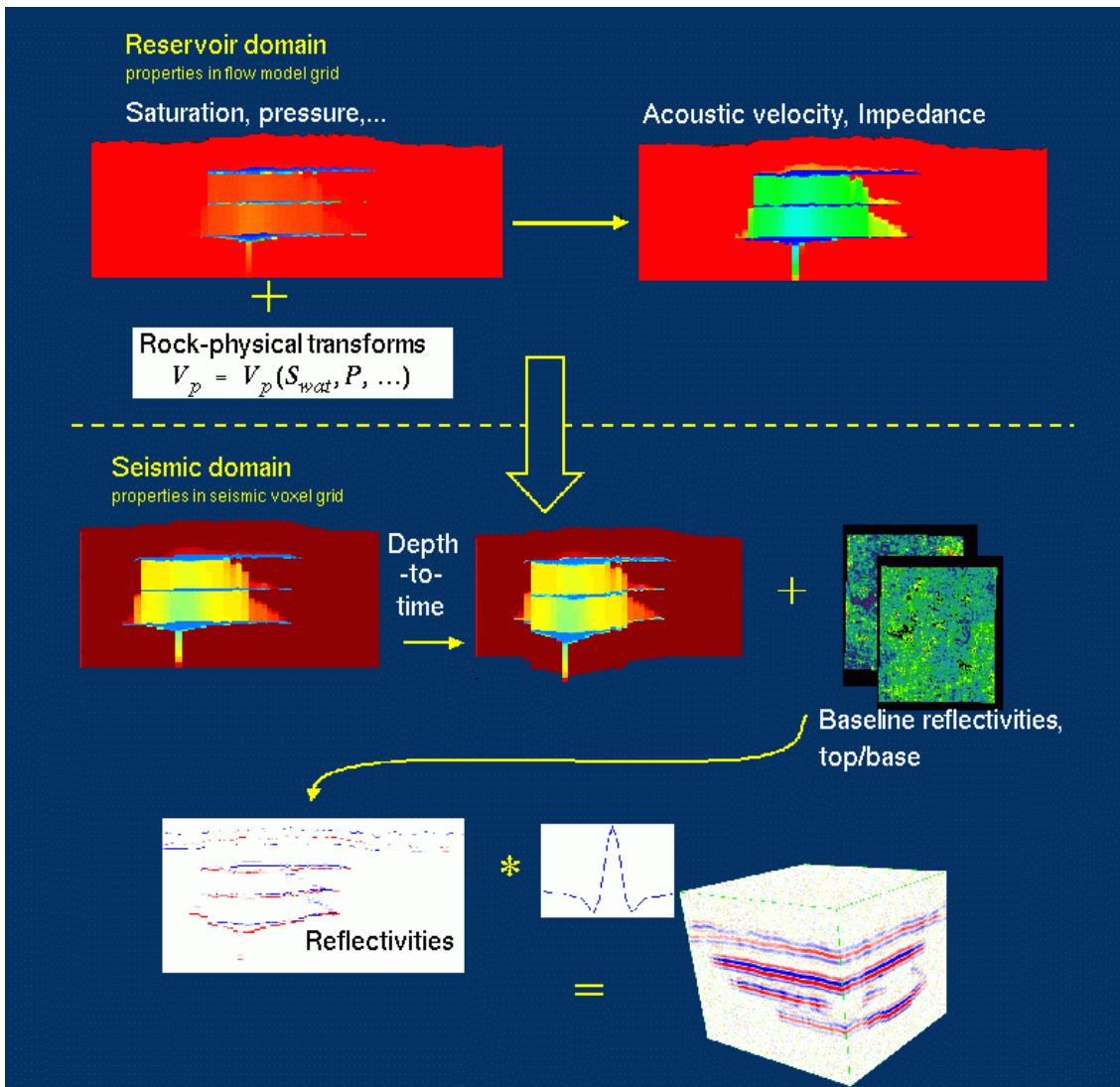Figure 55 Optimisation loop for matching flow models with 4D seismic.

Figure 56 Flow diagram for the generation of synthetic seismic.

In the study by Lindeberg *et al.* (2000) a particular focus was to investigate the mechanisms for transport of CO_2 through the shale layers. These layers can either be semi-permeable leading to a dispersed flow between the layers, or the layers can be sealing with localized holes conducting the CO_2 in columns. In the first case, more water will be in contact with the CO_2 giving rise to a larger portion of the CO_2 being dissolved in the water than in the second case. The question of how much CO_2 is dissolved in water is essential to address in order to predict the long-term fate of the CO_2.

A particular problem in the current project is the evaluation between the 4D seismic and the predicted CO2 distribution. Parameters in the rock-physical model are uncertain leading to ambiguities in the relations between the observed seismic and simulation results. It is also possible for different reservoir flow models to predict the correct number of clouds and approximately the same lateral extension of the individual clouds. Additional observations in order to distinguish between different possible flow models are therefore needed. The presence of CO_2 introduces a reduction in compressional wave velocity resulting in an increase in travel-times for reflections below the CO_2. This pull-down can be observed and quantified from the time-lapse seismic. A forward modelling of acoustic properties is here performed from the flow model and the modelled pull-down is compared to the observed pull-down. This evaluation will both reduce uncertainties associated with the flow model and uncertainties in the rock-physical transforms. In order to differentiate between different flow models, a method for generating synthetic seismic responses has

therefore been developed. The remaining part of this section is therefore used to describe this method, and how derived data, including calculations of synthetic pull-down is used in the evaluation of the flow models.
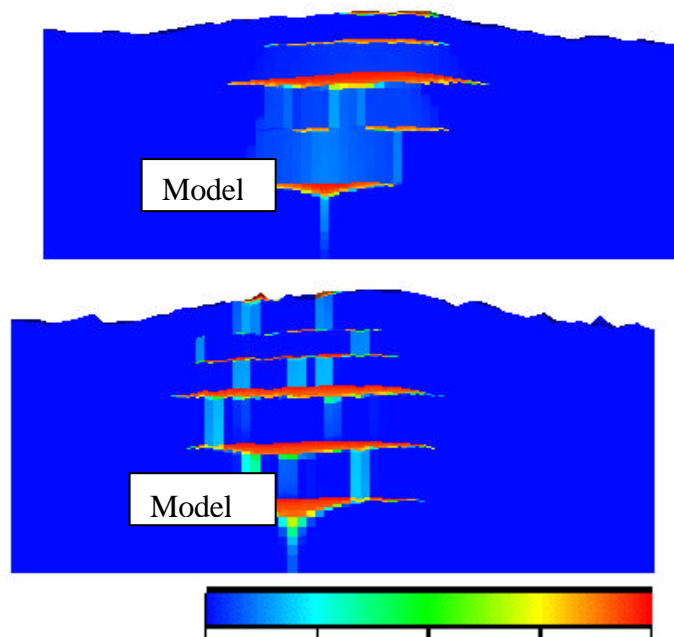

Figure 57 Cross-sections of predicted CO_2 saturation in 1999 from Model I and Model II.

Method for generating synthetic seismic

The procedure for generating synthetic acoustic properties and synthetic seismic is illustrated in Figure 56. Key elements are

- Generation of acoustic impedance and velocity on the flow model grid using a rock-physical transformation
- Domain transformation from the flow model grid into a voxel cube grid
- Using the synthetic acoustic velocity in the voxel cube, a depth-to-time conversion is made
- Reflectivity maps are used to generate the impedance above and below the reservoir. The reflectivity $r_t(x, y)$ and $r_b(x, y)$ at the top and base of the reservoir are detected from the seismic of the base-line survey using a statistical deconvolution algorithm (Nickel et al.). The impedance $Z_t(x, y)$ in the over-burden is then calculated from the formula

$$Z_t(x, y) = \frac{1 - r_t(x, y)}{1 + r_t(x, y)} \cdot Z(x, y, z_{top})$$

where $Z(x, y, z_{top})$ is the synthetic impedance just below the top reflector of the reservoir.
- Correspondingly the impedance below the reservoir is calculated.
- From the impedance-cube, which now covers both the reservoir and the regions above and below, reflectivities are calculated

The statistical deconvolution algorithm (Nickel et al.) extracts a global wavelet from the real seismic. This wavelet is then convolved with the reflectivity-cube to produce a synthetic seismic cube.
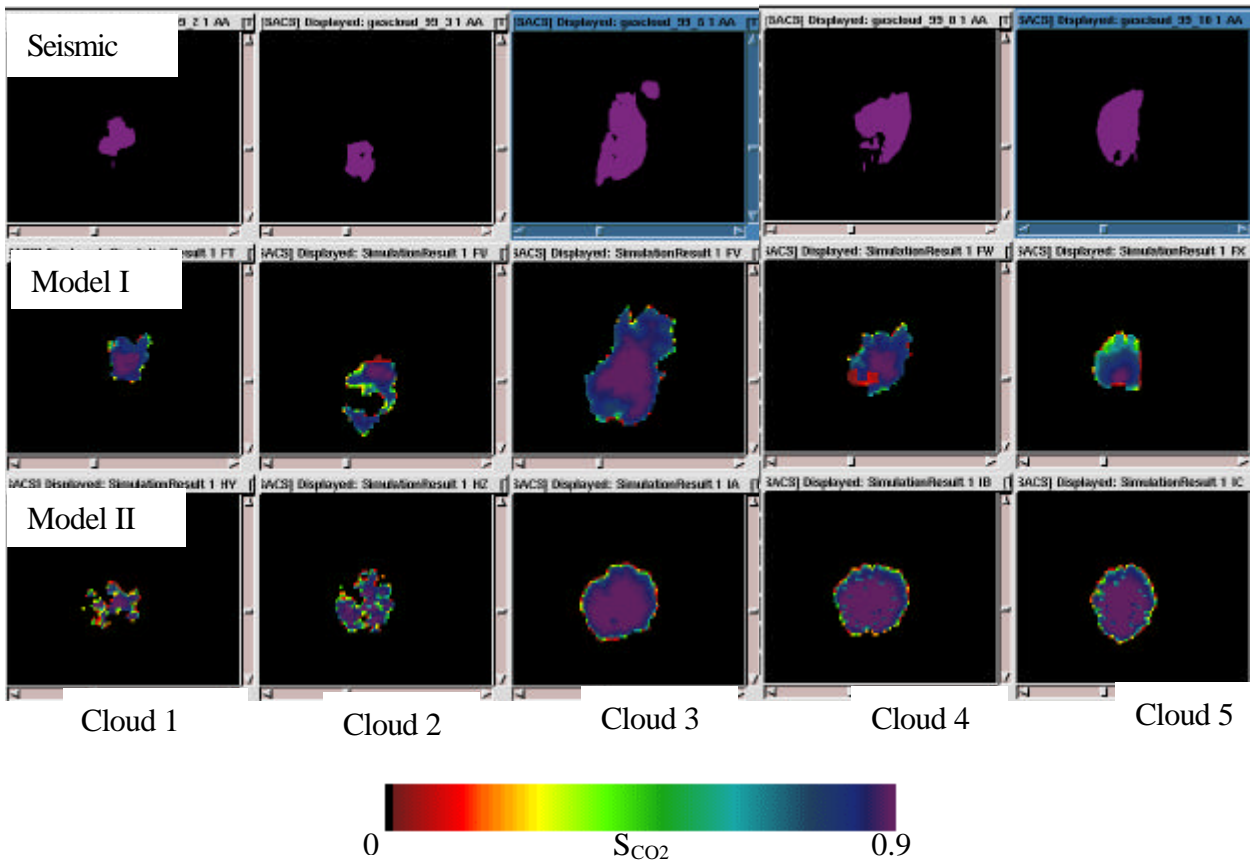
Figure 58 Images of the 5 simulated CO2 bubbles in the Utsira sand and the corresponding interpreted "clouds" observed by the 1999 seismic. Cloud 1 is at the top of the sand, while Cloud 5 is closest to the injector well. The 5 lowest images are from Model II while the images in the middle are from Model I. The clouds observed from the seismic are given by the interpreted extension of the individual clouds, while the modelled clouds are given by the saturation just below the shale layers.

Figure 59 P-velocity in depth and in time after a depth-to-time conversion. Data is from Model I.

Reservoir flow models

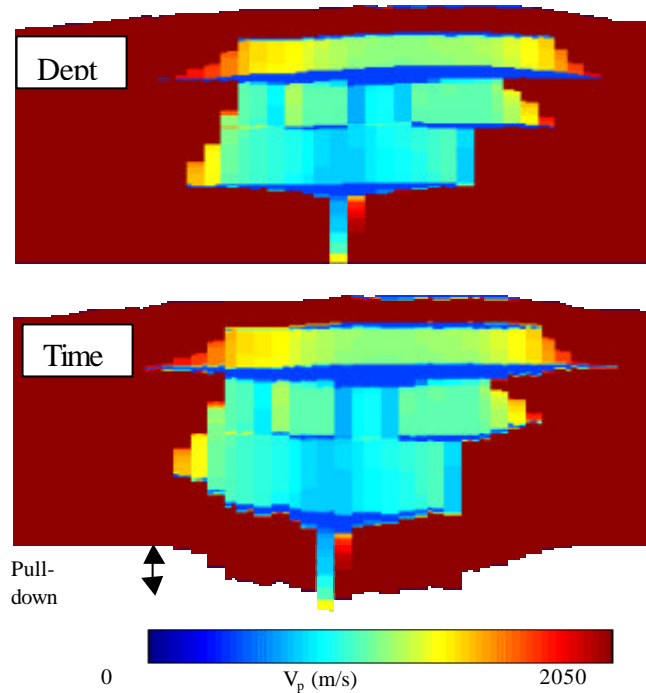Two versions of the 3D flow model Lindeberg (2000) have been investigated, both consisting of 428 400 grid cells. Transmissibility multipliers have been used to model the effect of the shale layers. In one model the shale layers are semi-permeable and in addition the layers contain one or two high-permeable holes. Initially this model did not predict the correct number of CO_2 clouds. By modifying the size and location of the individual holes, and in addition the depth contour of one of the shale layers, a satisfactory match was obtained. Hereafter this matched model is denoted Model I. In the second model, denoted Model II, the layers are impermeable except for a higher number of holes in each layer (about 300). The position of the holes in Model II is stochastically distributed. In both models the CO_2 gets trapped below the shale layers. However, the distribution of CO_2 in the sand between the layers is very different in the two models, as seen in Figure 57. The lateral extensions of the clouds are compared to the seismic observations in Figure 58. It is seen that the size of the modelled clouds is approximately equal to the seismic observations. The shape of the clouds is not completely reproduced. The main reason for this is that the contours of the shale layers are not known, and the modelled shale layers are parallel to the Top Utsira contour.
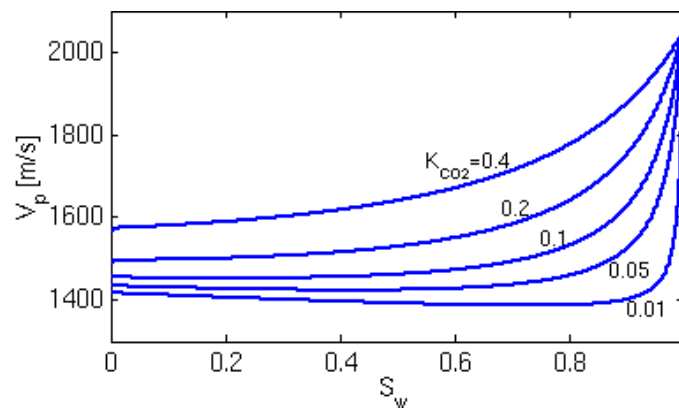

Figure 60: Gassmann-modelled seismic velocity V_p in CO_2-water system as function of the water saturation S_w. The density of the CO_2 is 650 kg/m^3. The bulk modulus of the CO_2 is varied from 0.01 to 0.4 GPa.

The rock-physical modelling is based on the Gassmann equation. The input parameters used have been determined from well log data by Arts *et al.* (2002). The density of the CO_2 under reservoir conditions is about 650 kg/m^3. The acoustic velocity is highly sensitive to variations in the CO_2 bulk modulus, see Figure 60. In our study the value of the CO_2 bulk modulus is varied according to the uncertainties in this parameter. From Figure 60 it is seen that when K_{CO2} is low, even small values of the CO_2 saturation leads to a large drop in the velocity. Consequently, a flow situation with low-saturated CO_2 between the accumulations can lead to a very strong pull-down if K_{CO2} is low. This is indicated in Figure 59 where the pull-down from the model is given from the depth-to-time conversion.

There are different ways to measure the pull-down from seismic signals. One method is to cross-correlate the seismic signals between the seismic surveys, using only the signals from below the injected CO_2 (Arts *et al.*, 2002). Also, direct interpretations of seismic horizons below the CO_2 can be compared, as indicated in Figure 51. These two methods give the integrated time-delay caused by the total volume of injected CO_2.
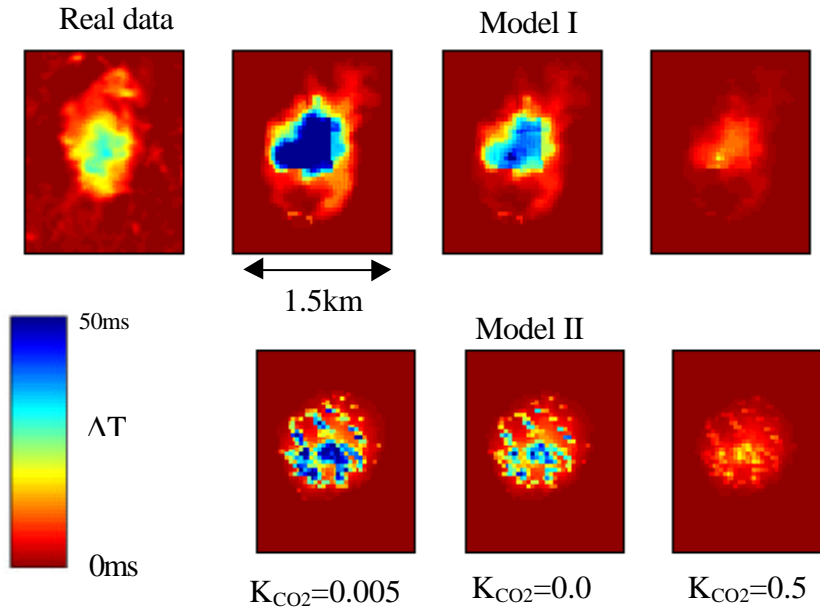
Figure 61: Comparison between real and synthetic pull-down using three different values of the K_{CO2}. From the 1999 data. The pull-down is measured in TWT. The three upper synthetic images are generated from Model I while the three lower are from Model II.
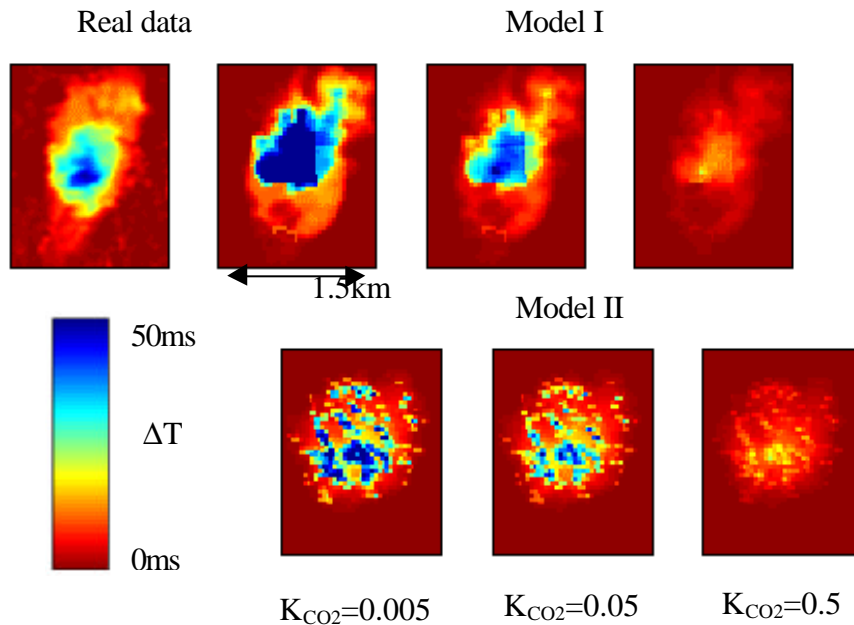

Figure 62: Comparison between real and synthetic pull-down from the 2001 data.

Results

Maps showing the interpreted pull-down (two-way-time) measured by the seismic in 1999 and 2001 are shown in Figure 61 and Figure 62. It is seen that the basic shape of the pull-down is similar for the two measurements, but the pull-down has increased and the 3D volume affected by the pull-down has been extended due to the additional CO_2 injected between 1999 and 2001. In the same figures synthetically generated maps of the pull-down are given. In order to incorporate uncertainties associated with the rock-physical transformations, three different values of K_{CO2} are used. There are uncertainties associated with other parameters in the rock-physical model as well, but the variation of the bulk modulus has the largest impact on the present results. And in order to evaluate the migration mechanisms of the CO_2, data from the two models are used. It is seen from Figure 61 and Figure 62 that neither of the synthetically generated

pull-down-maps capture the exact shape of the map based on real data. The pull-down from Model II varies quite rapidly laterally in contrast to the real pull-down. The high-valued peaks of the pull-down from Model II are caused by the vertical columns of CO_2 above the high-permeable holes in the shale layer. In Model I the variation of the pull-down is smoother due to the presence of low CO_2-saturated rock in the region between the shale layers.

In order to quantitatively compare the synthetic and real data, a "pull-down-volume" is calculated. This volume is the area integral of the pull-down, and is hence a quasi-volume with unit m^2s. The results are shown in Figure 63 where a continuous range of K_{CO2} is used. Based on both the 1999 and 2001 data it is seen that for most values of K_{CO2} the pull-down from Model II is underestimated. Only for very low values (<0.005) of K_{CO2} the observed pull-down-volume is reproduced.
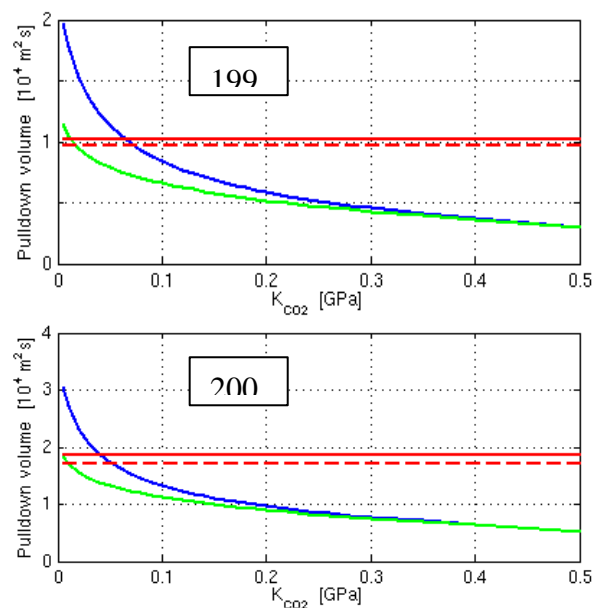

Figure 63: Pull-down-volume from Model I (blue), Model II (green) compared to observed values from direct interpretation (solid red) and from cross-correlation (dotted red, Arts et al. in press). 1999 and 2001 data.

Inline sections of synthetic seismograms are given in Figure 64. Even though there is not an exact match, the seismic from Model I reproduce the dominant features of the real seismic. In contrast, Model II gives a more noisy pattern due to the strong lateral variations caused by the vertical columns of CO_2. The strong variations in the seismic from Model II indicate that more advanced modelling, incorporating diffraction effects, could be used in generating synthetic seismic from Model II.

Discussion and conclusions

Based on the results, Model II, which transports the CO_2 in distinct vertical columns between the shale layers, give too small pull-down. The CO_2 columns are also strongly reflected in both the pull-down and the synthetic seismic. This is not observed in the real seismic. The low CO_2-saturated rock between the shale in Model I, on the other hand, give a stronger pull-down. The lateral variation of the pull-down and the synthetic seismic is also in agreement with the real observations.

It may therefore be concluded that it is unlikely that the CO_2 is solely transported through a set of distinct holes in the shale layers having the size of the simulation grid cell (about 30 x 30 m). The shale layers
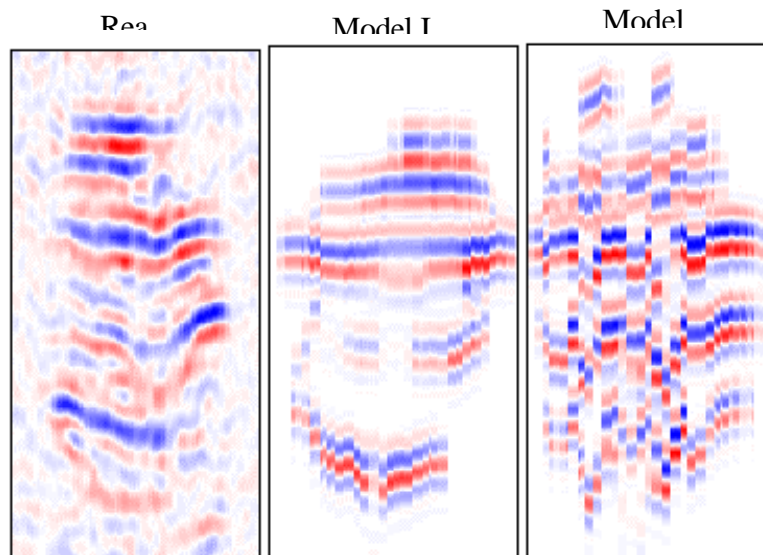
Figure 64: Seismic difference images from real and synthetic data.

therefore seem to be either semi-permeable, or they may have a more dense distribution of holes of a smaller scale than the simulation cells.

The 4D workstation software development

The 4D Workstation project was initiated with the primary goal of integrating existing 4D functionality and to identify and implement functionality needed for a more streamlined workflow. New functionality has been written using Java and OpenSpirit in order to take advantage of developments in both programming technology and distributed data access. Elements of the 4D workstation are being developed within the SACS2 project. However, in this section the entire workstation is described for completeness.

The Launcher

The need for an integrating launcher resulted in the 4D Workstation application launcher depicted in Figure 65. It is a one click Java WebStart launcher and, for newer Java-based applications, also offers one click deployment. This means that the user will always have access to the latest version of the software every time the application starts.

If we examine Figure 65 more closely, we see a mix of familiar GeoFrame applications and quite a few new ones. The workflow starts with a Repeatability Assessment phase, and then enters the main reservoir optimisation loop, consisting of geometry extraction, attribute extraction, classification and then reservoir optimisation. As a part of the reservoir optimisation phase, fluid substitution could be performed in order to better understand the seismic response.

Software and data access

In order to make the 4D Workstation software as accessible as possible, we decided to use the Java programming language for all new developments. Not only has Java shown a marked increase in programmer productivity, but programs also tend to have a lot less bugs. In addition to this, Java has a large toolbox available. This makes many tasks trivial that would have required a substantial effort in other programming languages like C++.
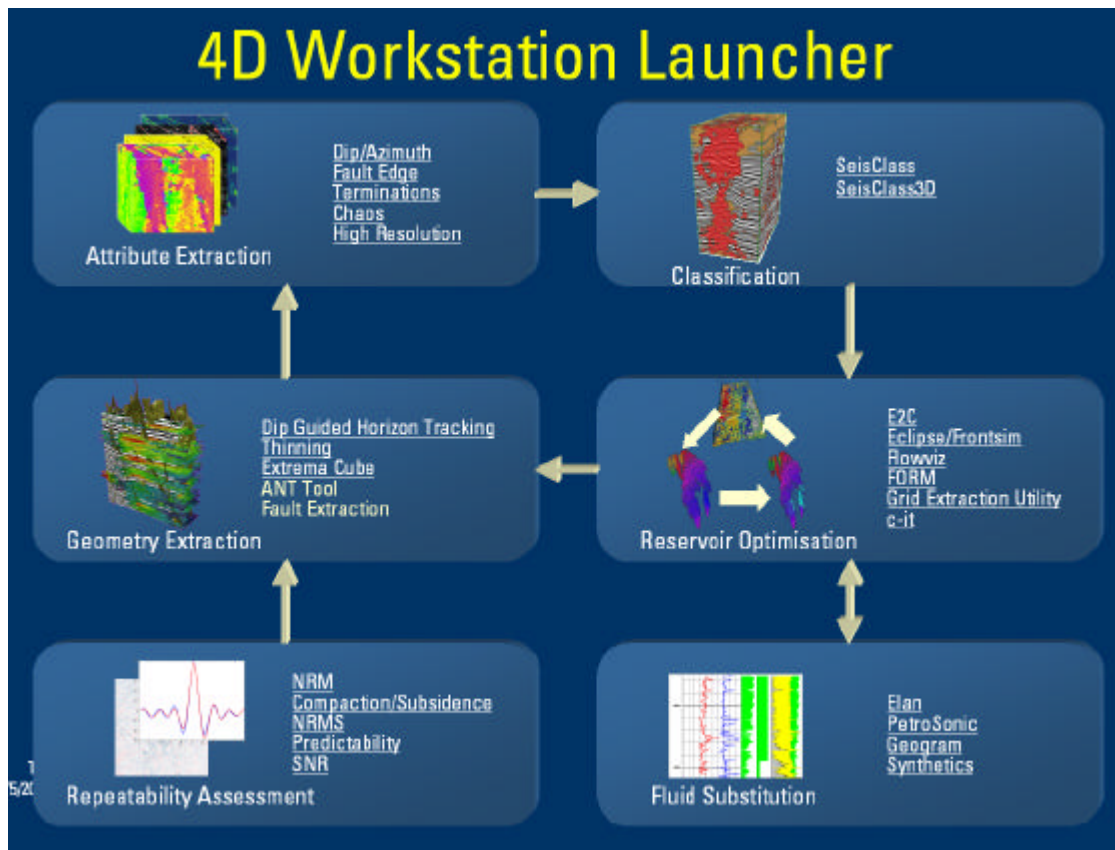
Figure 65 The 4D Workstation Launcher

When it comes to data access, we choose to implement a simple layer of business objects that model seismic entities like seismic cubes, horizons, well-trajectories and well-logs, in addition to reservoir entities like reservoir simulation grids and flow-lines. This layer was named RAPID (Research API for Development) and has been mapped to several physical databases through the OpenSpirit framework, but also directly to flat files (including Eclipse and FrontSim) and GeoFrame. The RAPID architecture is shown in Figure 66. At the bottom of the figure we see the server side with the currently implemented databases, or backends as they are usually called. We see that both GeoFrame and Landmark are available through the commercial OpenSpirit server. In addition to this, we have made a direct link to GeoFrame, as this is easier to use in an environment where GeoFrame is already installed. We also have a flat file backend that allows a user to mirror any of the other RAPID enabled backends into a file directory and also select for which data entities the bulk data should be downloaded. The user can then, as an example, take these data onto a portable PC and run RAPID-enabled software like if it was against a live database. If data items or bulk data are created/updated, these changes can be transferred back as soon as the user hooks the portable PC back onto the required network. The benefit of a flat file backend when doing developments and debugging, is also self-evident.
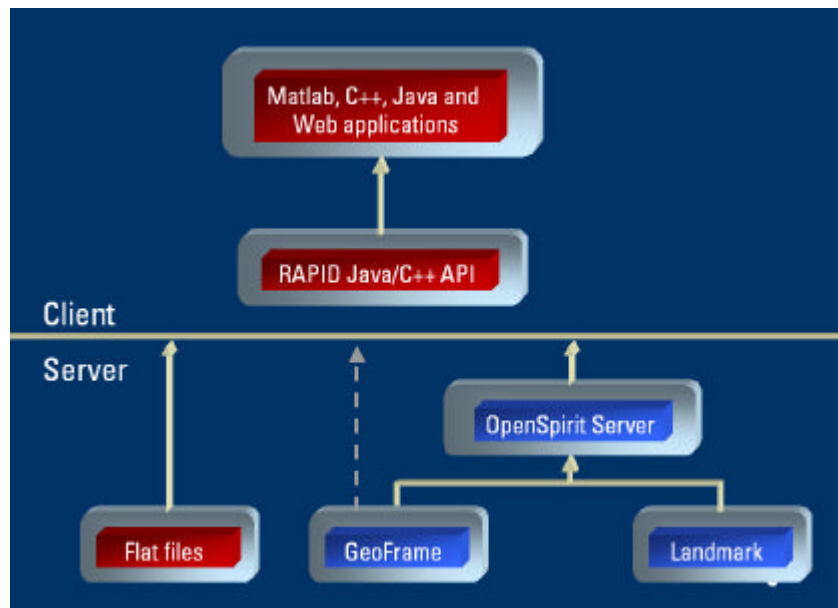
Figure 66 The RAPID architecture

We have also implemented a Matlab binding for the RAPID API. This means that database access is now available for rapid prototyping. For simple Matlab applications, it is even possible to automatically generate standalone executables directly from the Matlab scripting language, complete with OpenSpirit data access.

The client application will get all its data through RAPID, and will in effect don't know (or care for that matter) where the data came from physically. For a developer this provides a nice abstraction, and greatly simplifies coding. RAPID is available in a multi platform Java version, and also as a C++ for both Microsoft Windows and Sun Solaris.

Batch Oriented Processing

The traditional approach to attribute generation has been to compute attributes one by one in a sequential fashion. The user would then monitor the progress in order to be ready to start the next attribute generator. For some of the attributes, it takes hours and even days to compute a seismic cube, and normally something like 20 attributes are computed, so this is clearly and area where throughput should be increased. Hence, there is a significant a need for batch-oriented processing applications. We initially set out to make a multithreaded[3] attribute generator for all of 1D (well-logs), 2D (horizons) and 3D (seismic) data. This computation of attributes, especially for 3D data, is so time consuming that it is not realistic to do this on the fly when the attributes are needed, but rather compute the attributes up front and store them persistently in the database.

---

[3] A multithreaded application can run several tasks at the same time, like running a lengthy processing task in the background while the user still can use the application interactively.
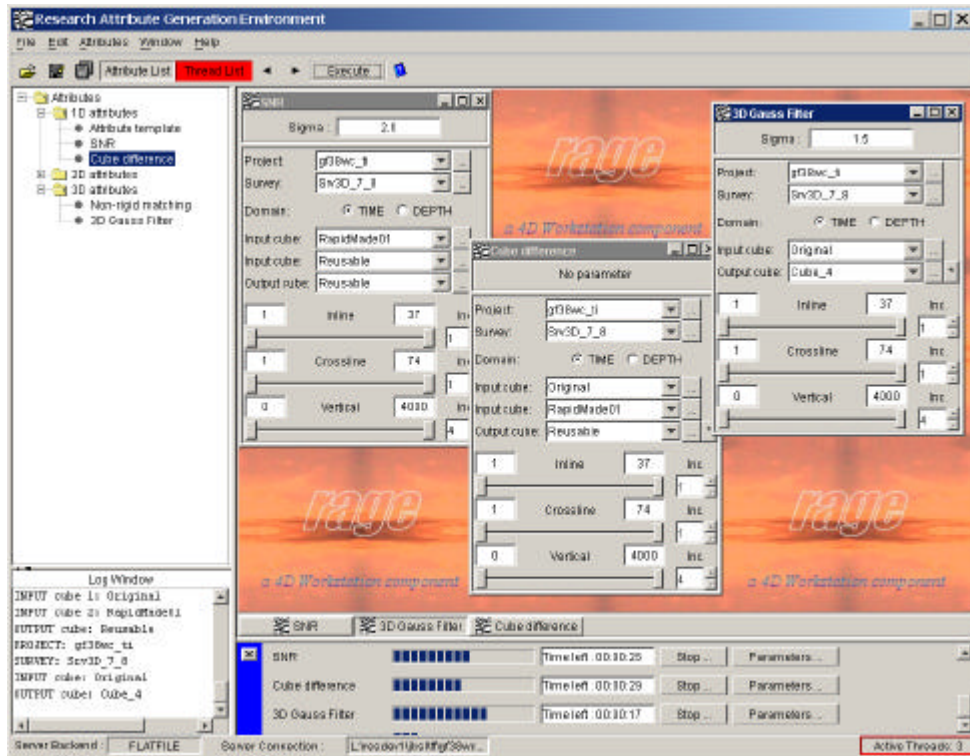
Figure 67 A screenshot of the RAGE user interface.

To streamline the attribute generation process, we developed the RAGE (Research Attribute Generation Environment) application as shown in Figure 67. In the top left window, the user selects an attribute generator from the tree structure, and this will open a new window in the main work canvas on the right where the user can choose data items and set parameters. The user can also select, and switch, which RAPID backend he wants to work on, so data can be read from all available backends without restarting the application. The figure shows three simple attribute generators, and the status windows below the main work canvas shows the progress of the three attribute generators running simultaneously. On a multiprocessor machine, the processes started in RAGE will spread out evenly on the available processors thanks to the built-in load balancing mechanisms of Java. RAGE has also been extended from its initial scope of attribute generation to also cover more aspects of the workflow. If we look back at Figure 65, RAGE now covers applications from the three boxes on the left, feasibility assessment, geometry extraction and attribute extraction.

We have also included 2D viewers for seismic and horizons, so that the user can check the results of a process without having to switch to a visualization application. Future enhancements will include visualization of well logs. It would also make sense to add the 3D viewer, described next, directly into the RAGE framework. Adding to this, we also plan to include a batch queue, and possibly a save option for a set of process parameters in order to facilitate a rerun of the processes in the future.

3D Visualization

Traditional G&G 3D visualization applications have not been able to integrate data entities from both the seismic domain and the reservoir domain. This functionality would be especially useful in a 4D setting where the user wants to switch back and forth between the two domains during an iterative workflow as the one outlined in Figure 65. In order to empower the user with multi domain visualization, we developed a set of visualization framework components called *c-it*. There is one component for each of seismic, horizons, well traces, reservoir model grids and flow-lines. The *c-it* framework is written in Java3D and will as such run on any platform supporting the Java3D runtime, like PC's (Windows and Linux), Sun Workstations or

even SGI high end visualization systems. Somewhat surprisingly, we found that the latest generation of PC graphic cards perform very well, and in many cases better than their more expensive workstation counterparts. The big driver here is of course the 3D game playing market. Unfortunately this means that some types of functionality, that would benefit scientific visualization, are lacking, notably 3D textures and stereo viewing capabilities.

Automatic Geometry Extraction and Editing

Automatic geometry extraction is a crucial part of our 4D workflow, and occupies one of the main boxes in Figure 65. We have built two new applications for automatic interpretation of primarily faults, even though the methodology is applicable to horizons as well. The AntTrack application does the automatic extraction of surface patches, and the Structural Geology Editor (SGE) is used for visualization and interactive editing the retrieved fault patches. The AntTrack user interface is depicted in Figure 68. The polar plot on the right lets the user select the azimuth and dip intervals the algorithm should consider when doing the fault extraction.
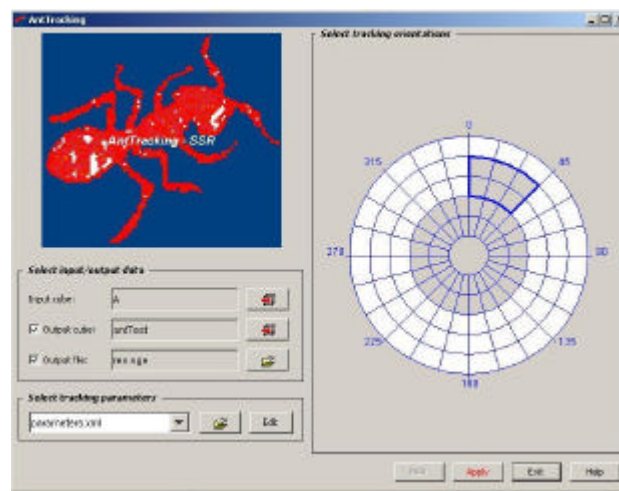

Figure 68 The AntTrack user interface

The Structural Geology Editor (SGE) is show in Figure 69 and Figure 70, where the user has selected two nearby patches (marked in red in Figure 69), and has then performed a merging operation (marked in red in Figure 70). This is a very intuitive way of working for most users, and is inspired by image editing software paradigms. The SGE is built using c-it components, so only the selection and merging mechanisms had to be added.
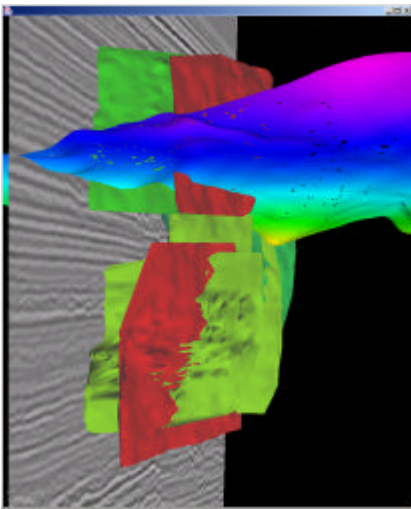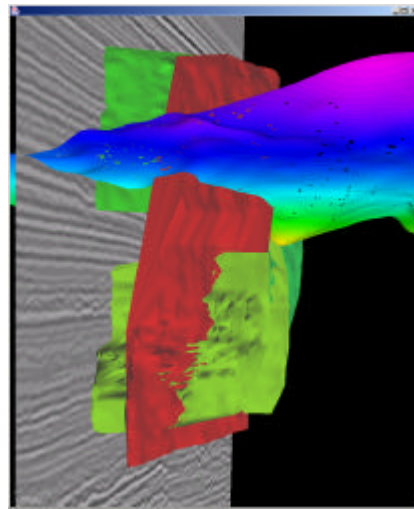
Figure 69 SGE with selected patches in red   Figure 70 SGE with merged patches

Eclipse data extraction utilities

In Figure 65, we see that our 4D workflow is cyclic and that we can iteratively switch between the simulation domain and the seismic domain. We have made a utility to extract any type of information from an Eclipse simulation file into a RAPID enabled database. The user is able to preview the extracted information graphically, and will then generate the persistent database entries when desired. A screen shot of the Eclipse extractor is show in Figure 71.
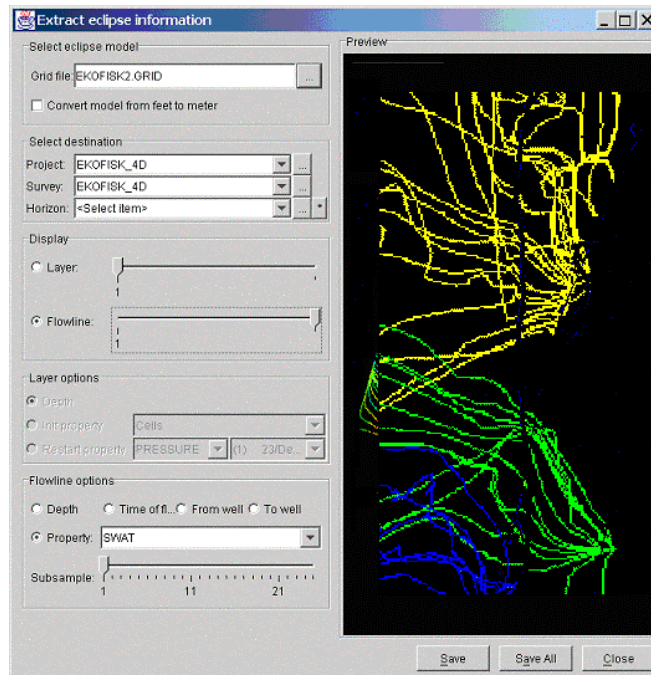

Figure 71 The Eclipse grid extractor

Conclusion

Many important applications have been built to make 4D workflows easier, and the first steps towards a tighter integration of the various components have been taken. We will continue this work towards our vision of one integrated solution for the whole 4D workflow, giving our users state of the art tools to significantly reduce the effort involved in taking on advanced 4D studies. This tool set is expected to

significantly improve the workflow throughput also in CO2 injection monitoring, and the so far developed functionality already delivers a significant improvement over older tool sets.

References

[1]   Ivar Brevik, Ola Eiken, Rob Arts, Erik Lindeberg and Emmanuel Causse, *'Expectations and Results from Seismic Monitoring of CO2 Injection into a Marine Aquifer'*, EAGE 62nd Conference and Technical Exhibition, Glasgow, Scotland, 29 May - 2 June 2000, article B-21.

[2]   Ola Eiken, Ivar Brevik, Rob Arts, Erik Lindeberg, Kjetil Fagervik*, 'Seismic Monitoring of CO2 injected into a marine aquifer'*, SEG 2000, Calgary, Canada, August 2000.

[3]   Ulrik Gregersen, Olaf Michelsen and Jan C. Sørensen, '*Stratigraphy and facies distribution of the Utsira Formation and Pliocene sequences in the northern North Sea'*, Marine and Petroleum Geology, Vol. 14, No. 7/8, pp. 893-914, 1997.

[4]   Zweigel, P., Hamborg, M., Arts, R., Lothe A., & Tømmerås, A., 2000: Prediction of migration of CO_2 injected into an underground depository: Reservoir geology and migration modelling in the Sleipner case (North Sea). 5th International Conference on Greenhouse Gas Control Technologies, Cairns (Australia).

[5]   Lindeberg, E., Zweigel, P., Bergmo, P., Ghaderi, A. and Lothe, A., 2000: Prediction of CO_2 dispersal pattern improved by geology and reservoir simulation and verified by time-lapse seismic. 5th International Conference on Greenhouse Gas Control Technologies, Cairns (Australia).

[6]   Fagervik, K., Lygren, M., Valen, T.S., Hetlelid, A., Berge, G., Dahl, G.V., Sønneland, L., Lie, H.E. & Magnus, I., 2001: A Method for performing History Matching of Reservoir Flow Models using 4D Seismic. Society of Exploration Geophysicists 71th Annual Meeting, San Antonio (Texas).

[7]   Arts, R., Elsayed, R., van der Meer, L., Eiken, O., Ostmo, S., Chadwick, A., Kirby, G., Zinszner, B., 2002: Estimation of the mass of injected CO2 at Sleipner using time-lapse seismic data. 64th EAGE Annual Conference & Exhibition, Florence (Italy).

[8]   Arts, R., Chadwick, R.A., Eiken, O., Kirby, G.A., Lindeberg, E. and Zweigel, P. (in press). 4D seismic imaging of a CO2 bubble at the Sleipner Field, central North Sea. In: Davies, R., Cartwright, J., Stewart, S., Underhill, R. & Lappin, M. (eds.) 3-D Seismic Data: Advances in the Understanding of Stratigraphic and Structural Architecture. Special Memoir of the Geological Society, London.

[9]   M. Nickel et al.: "A 3D stochastic approach for seismic reflector detection", Society of Exploration Geophysicists Extended Abstracts 1999.

[10]   M. Lygren, E. Lindeberg, P. Bergmo, G.V. Dahl, K.Å. Halvorsen, T. Randen and L. Sønneland: History matching of CO_2 flow models using seismic modeling and time-lapse data. Society of Exploration Geophysicists 72th Annual Meeting, Salt Lake City (Accepted).